Politecnico di Torino

Master of Science in Mechanical Engineering

Master Degree Thesis

Output-only operational modal analysis for cumulative seismic damage tracking in reinforced concrete structures

Supervisors:
Prof. G. C. Marano

Candidate:
Mahsa Daneshi Mamaghani

Student's ID:
S289497

Co-supervisors:
Prof. Quaranta Giuseppe
Ph.D. Marco Martino Rosso

December 2025
A.Y. 2025/2026

Abstract

This thesis investigates output-only dynamic identification for monitoring damage evolution in full-scale, three-dimensional, single-bay, three-story reinforced-concrete (RC) buildings subjected to shaking table tests, and evaluates the effectiveness of seismic retrofitting. Two nominally identical RC frames, one as-built and one retrofitted, were evaluated under controlled laboratory conditions. The frames were subjected to repeated low-level white-noise excitations, alternating with earthquake records of increasing intensity, using dense accelerometer instrumentation on both structures. The data were then reoriented to a common frame, time-aligned, uniformly resampled, and anti-alias filtered to make them suitable for modal analysis. Modal parameters at each stage were estimated using Frequency-Domain Decomposition in combination with covariance-driven Stochastic Subspace Identification as part of the operational modal analysis. To evaluate robustness and reproducibility, the complete identification workflow in Python (PyOMA2) and MATLAB (OoMA Toolbox) for cross-validation. Reference properties for comparison were provided by a finite-element baseline implemented in the Scientific Toolkit for OpenSees (STKO) software. The results reveal clear, progressive stiffness degradation with increasing seismic excitation in both specimens. In the case of the retrofitted building, a stiffer response was observed, which highlights the effectiveness of the retrofit. Damping estimates continued to fall within the ranges reported for similar RC frames, and agreement between experimental results and numerical models remained strong. Although mode-shape estimates did not perfectly match the finite-element predictions, the Modal Assurance Criterion (MAC) showed well-separated principal modes and stable consistency across tests. That suggests the identification was physically meaningful even if some local differences were present. Residual differences are possibly due to sensor layout, mild nonlinear effects under stronger inputs, and modeling simplifications. The work presents a reproducible workflow from sensing and preprocessing to identification and validation and provides practical recommendations for monitoring cumulative earthquake damage in buildings, including guidelines on sampling, decimation, and model stabilization choices for robust OMA-based tracking.

.

Acknowledgements

First and foremost, I would like to sincerely thank my supervisors, Prof. G. C. Marano and Prof. Giuseppe Quaranta. Not only did their guidance, encouragement, and insightful feedback throughout my thesis support me, but their expertise and steady support also played a key role in shaping this work and helping me develop as both a researcher and an engineer.

I am especially grateful to the PhD. Marco Martino Rosso, with whom I had the honor of working closely each day. His patience, availability, providing an environment to work more effectively, and practical advice were invaluable at every stage of the project, from our initial discussions to the final results. Learning from his experience and enthusiasm has truly been an honor.

I would also like to thank my beloved family for their persistent support and for always believing in me, even from afar. Finally, a special tribute must be dedicated to my partner, whose patience, support, understanding, and love have been a constant source of strength and motivation throughout this journey.

Contents

List of Figures

List of Tables

Chapter 1

Introduction

1.1 Background & Motivation

Earthquakes impose substantial human and economic losses, and reinforced concrete (RC) frame buildings have a significant share of the at-risk stock in seismic regions [1]. In many countries, much of the RC inventory was built using older force requirements, and these did not include clear performance goals; as a result, the true in service behavior of these buildings, especially under sequences of mainshock–aftershock events, may depart from design assumptions. Timely, non destructive assessment of their dynamic properties, natural frequencies, damping ratios, and mode shapes is central to performance based evaluation, rapid post event triage, and the prioritization of retrofit actions [2].

Operational Modal Analysis (OMA) makes it possible to estimate modal parameters by relying solely on response measurements obtained during naturally occurring, random excitations such as ambient vibrations and everyday operational loads [1, 2]. In contrast to Experimental Modal Analysis (EMA), which requires applying controlled forces and often means taking a building out of service, OMA can be carried out while the building is still being used as normal. This practical advantage is a key reason why OMA has become so widely adopted in structural health monitoring (SHM) [2]. The early detection of stiffness changes through frequency shifts is possible through tracking modal properties over time, which facilitates the identification of potential damage progression, and informs updates to digital twins and finite-element (FE) models for making decisions about retrofits and continued building use [3].

OMA has been transformed into an intelligent system through recent advancements which is recognized as automated OMA (AOMA) system. These systems use pipelines that continuously gather data, analyze it, remove the influence of environmental and operational changes, and send alerts with clear confidence levels [4, 5].Essential factor not only for efficiently expanding monitoring to cover buildings but also for reducing false alarms caused by factors such as temperature, humidity, or building occupancy is automation [4]. The integration of OMA with data-driven techniques, such as quality

control, advanced statistics, and machine learning, has influenced how we monitor and manage civil infrastructure as a part of SHM [4, 5].

From a risk management point of view, OMA offers two main benefits. First, before an event happens, OMA enables the creation of solid baseline measurements and variability ranges for important modal parameters. After an event, it enables the rapid detection of statistically significant changes from these baselines. This enables more effective prioritization of inspection resources and supporting informed decisions about whether buildings can be safely reoccupied or need to be cordoned off [2]. These practical applications provide the motivation for the methodological and comparative review that follows and shape the core objectives of this thesis.

1.2 State of the Art in Dynamic Identification & SHM

Stochastic subspace identification (SSI) and frequency-domain decomposition (FDD) are the two primary methods that operational modal analysis (OMA) most frequently employs when examining entire buildings.[2]. In FDD, the power spectral density matrix $S_{yy}(\omega)$ is examined at each frequency using singular value decomposition. Natural frequencies appear as peaks in the leading singular value, while the corresponding singular vectors provide initial mode shape estimates. Enhanced Frequency-Domain Decomposition (EFDD) can be used to estimate damping by inverse-transforming a narrow frequency band and examining how the signal decays over time; however, these damping estimates are typically less consistent than frequency estimates. In the covariance-driven stochastic subspace (SSI) method, outputs are mapped into block Toeplitz or Hankel structures in order to estimate a state-space model. The discrete poles λ_i are then transformed into continuous parameters via $s_i = \frac{1}{\Delta t}\ln(\lambda_i) = \sigma_i + j\omega_i$. The corresponding natural frequency is $f_i = \frac{\omega_i}{2\pi}$ and the damping ratio is $\zeta_i = -\sigma_i/\sqrt{\sigma_i^2 + \omega_i^2}$. Stabilization diagrams are used to determine poles that are consistent in frequency, damping, and mode shape over multiple model orders. [2, 5]

Practically, operational modal analysis (OMA) is frequently paired with finite-element (FE) models. This approach allows to consider shifts in frequency as signs of changes in stiffness, understand the roles and influences of different mode types and assess how well retrofits are working in existing buildings [3]. Both lab and full-scale experiments serve as a complement to field studies, supplying controlled conditions and well-defined damage phases. Controlled setups enable researchers to monitor in detail how a structure's properties change with damage or successive earthquakes. To help discriminate damage levels, earthquake excitations are often alternated with white-noise segments. Accordingly, seismic records are interleaved with white-noise windows to delineate damage states while keeping the stochastic-input assumption for OMA valid in the identification windows [6, 7, 8].

Automated OMA (AOMA) pipelines enable continuous tracking of the health of structures over time. These systems automatically identify key modal properties, filter

out trends caused by changes in the environment or changes in how the building is used, measure uncertainty, and send alerts when they detect significant changes [4, 5]. The systems generally verify incomplete data and, using robust procedures such as Welch averaging, estimate the power spectral density (PSD). They follow how modal properties change over time relative to previous measurements and adjust models to capture slow shifts in frequency. In earthquake-prone regions, these systems adjust their thresholds after an event to enable engineers to quickly assess building safety [4, 1].

For monitoring, using dense networks of low-cost MEMS accelerometers is essential. This setup presents several challenges, including unsynchronized clocks, sensors that are oriented in different directions, and suboptimal sampling. Preprocessing is an important step prior to analysis, including aligning sensor channels to the same reference frame, applying anti-aliasing during resampling, and synchronizing to a single clock to minimize errors [10, 11]. After these steps, frequency estimates tend to be robust; nevertheless, damping ratios and mode shapes can still be impacted by noise, notably at low signal-to-noise ratio [2, 11].

1.3 Comparative Advantages and Limitations of Prevalent Techniques

OMA is a non-intrusive technique that can be deployed on structures in service without the need for controlled inputs. OMA is particularly effective for tracking frequency changes that indicate variations in structural stiffness over time [1, 2]. However, estimates of damping and mode shapes using OMA are more sensitive to noise [2]. In contrast, EMA (input–output testing) provides high-quality frequency-response functions (FRFs) and generally yields more reliable damping and mode-shape estimates when input conditions are well controlled. This level of reliability is obtained by utilizing dedicated excitation equipment, careful test planning, and accepting operational downtime, which is often impractical for buildings in operation [2].

FDD enables efficient peak picking and initial mode-shape identification, especially for closely spaced modes, with straightforward implementation and interpretation [2]. Its main limitation is that damping estimation is indirect, depends on additional assumptions, and is sensitive to band selection [2]. Covariance-driven SSI provides time-domain damping estimates and robust pole validation with stabilization diagrams; however, the results are sensitive to analyst-selected settings (block-row count, model order, window length, decimation). Hence, parameter robustness studies and multi-criteria stability checks are recommended [5, 11].

For distributed Micro-Electro-Mechanical Systems (MEMS) sensor arrays, adaptive synchronisation together with high-accuracy resampling is needed to mitigate interpolation-driven phase error and mode-shape bias. Synchronizing every sensor to

the same reference clock is necessary to maintain consistent causal ordering across channels [10]. Despite these steps, preprocessing can bias damping and mode-shape estimates more than frequency. Hence, it is important to incorporate redundancy (e.g., multiple channels per DOF), implement cross-checks via the Modal Assurance Criterion (MAC), and report uncertainties. [11].

Table 1.1: Typical decision criteria for selecting among identification techniques.

Task	**Preferred method**	**Why**	**Caveats**
Rapid screening / baseline update	FDD	Fast, simple peak picking; good for closely spaced modes	Indirect damping; sensitive to band selection [2]
Defensible damping & mode shapes	SSI-cov	Direct time-domain damping; stabilization checks	Parameter tuning needed (orders, rows, decimation) [5, 11]
Lab campaigns / controlled inputs	EMA / input–output	High-quality FRFs; strong damping identifiability	Requires shakers, downtime; less feasible in service [2]
Portfolio-scale monitoring	AOMA (FDD+SSI)	Automation, trend de-seasoning, alerting	Requires QA, uncertainty handling, false-alarm control [4, 5]

Modal-validation metrics help determine how consistent and reliable mode shapes are in structural dynamics. One common tool is the Modal Assurance Criterion (MAC), defined as

$$\mathrm{MAC}(\phi, \hat{\phi}) = \frac{|\phi^{\mathsf{T}} \hat{\phi}|^2}{(\phi^{\mathsf{T}} \phi)(\hat{\phi}^{\mathsf{T}} \hat{\phi})}. \tag{1.1}$$

A MAC value close to 1 indicates that the mode shapes are very similar. Typical stabilization criteria include MAC > 0.90 along with $|\Delta f|/f < 1\%$ and $|\Delta \zeta|/\zeta < 5\%$ [2, 5].

1.4 Research Gaps, Questions, and Objectives

Recent studies have demonstrated the feasibility of applying OMA to entire buildings; however, several key details remain unclear. For example, we do not yet know exactly how steps like orienting, syncing, or resampling data from MEMS sensors affect the results for damping and mode shapes. It is also unclear what the best, most reliable settings are for methods like FDD and SSI-cov, especially when it comes to reporting uncertainty. Lastly, comparing experiments with models is challenging when their

frequencies or the order of their modes do not match. These gaps complicate post-event decision-making and portfolio-scale monitoring [2, 10, 11].

To tackle these issues, this thesis poses five research questions:

(RQ1) Can we use changes in frequency to reliably track damage and relate it to the intensity of shaking, both in as-built and retrofitted buildings?

(RQ2) Does adding a retrofit always make a building stiffer when shaking is not too strong, and how does that benefit change as damage increases?

(RQ3) How much do the results for frequency, damping, and mode shapes change depending on how we process the data such as which filters or resampling methods we use, or how we set up SSI and which settings give the most reliable results?

(RQ4) How well can a simpler finite-element (FE) model explain what kinds of modes we see and how much they contribute, even if the actual frequencies are different? What is the best way to match up modes when their order changes?

(RQ5) How does the internal steel safety frame used in the laboratory influence apparent global stiffness (baseline frequencies) and, in particular, mode shapes (e.g., bending–torsion mixing and MAC degradation), and how should this bias be detected and accounted for during identification and interpretation? [2, 3, 11]

Based on these questions, the main goals are:

(O1) Create a repeatable process for working with dense MEMS sensor data ensuring correct sensor orientation, anti-alias filtering and uniform resampling, synchronization to a master clock, and quality checks at each step.

(O2) Estimate modal properties (frequencies and damping) using FDD and SSI-cov, report medians with 95% confidence intervals, and assess how sensitive these properties are to damage and shaking intensity.

(O3) Compare toolchains (PyOMA2 and OoMA) under matched settings, and report agreement metrics (Δf, $\Delta\zeta$, MAC).

(O4) Build a reduced-DOF FE baseline and use MAC-based pairing (even if mode orders swap) to interpret mode types and stiffness changes between the as-built and retrofitted buildings.

(O5) Quantify and control the influence of the internal steel safety frame by detecting frequency, damping, and mode shape bias at all intensity levels [2, 3, 4, 11].

1.5 Case Study and Dataset Overview

This thesis analyzes a controlled dataset from two full-scale, three-storey, single-bay reinforced-concrete (RC) buildings of nominally identical geometry and mass, both

anchored to a common RC base and outfitted with internal infills. One specimen incorporates a patented retrofit expected to increase global stiffness at the system level. The monitoring network comprises 40 MEMS sensing units (MonStr) that record triaxial accelerations; two units measure the input motion at the table and foundation, and 19 units per specimen are distributed across key structural nodes to capture floor and frame responses. White-noise windows alternate with scaled replicas of the 1980 Irpinia earthquake to bracket damage states and preserve the stochastic-input assumptions required for output-only identification. This design aligns with best practice in the literature where laboratory or full-scale campaigns interleave broadband excitations with earthquake records to support progressive-damage analysis and post-event assessments [6, 8, 9].

An internal steel safety frame was installed to protect the specimens and equipment during high-intensity runs. Comparing our measurements with an FE baseline that does not include this frame, we observe that even though the frame was mechanically decoupled as far as practically possible, local contacts and clearances modify the effective boundary conditions, adding stiffness and mass. The influence is most visible in the identified mode shapes, while baseline frequencies within white-noise windows are comparatively less affected. Accordingly, we interpret shapes with caution and base our primary SHM conclusions on frequency trends and cross-method consistency [1, 2].

The method used in this thesis centers on output-only operational modal analysis (OMA), making use of frequency-domain decomposition (FDD) and covariance-driven stochastic subspace identification (SSI-cov) methods. The analysis is carried out using the open-source PyOMA2 toolchain. The study prioritizes settings that are robust to parameter choices and provides clear reporting of uncertainty, while cross-validation is carried out in MATLAB with the OOMA toolbox. Identified modal parameters are interpreted against a finite-element (FE) baseline (OpenSees/STKO) to relate frequency shifts to apparent stiffness loss and to classify mode types and participation. This coupling of OMA and physics-based modeling reflects established practice for retrofit evaluation and decision support in building-scale SHM [1, 2, 11].

The thesis has practical boundaries that focus the contribution. An internal steel safety frame present in the laboratory setup may alter boundary conditions and mainly affect mode shapes rather than baseline frequencies in identification windows; this auxiliary interaction is acknowledged throughout the interpretation and sensitivity analyses. The retrofit is treated at the system level because proprietary details are unavailable, and the expected lower reliability of mode shapes relative to frequencies is addressed by redundant sensing, cross-method checks (FDD and SSI), MAC-based consistency thresholds, and FE cross-validation. These choices are consistent with recommendations in the OMA/SHM literature and with constraints typical of MEMS-based monitoring [1, 2, 11].

Chapter 2

Operational Modal Analysis

Operational modal analysis (OMA) is a field of study that involves techniques for dynamically identifying the modal properties of a structural system that is under ambient vibration, or, more generally, during its normal operating life. These methods rely solely on vibration response data; therefore, they are classified as output-only methods [12, 13]. The methods comprised by the dynamic identification process aim to identify the key parameters of a mathematical model that describes the structural system's dynamical behavior, so as to best fit the measured vibration responses collected during experimental campaigns [12]. Clearly, the observed vibration response reflects the physical properties of the structure being investigated, functioning as its concrete fingerprint. This aspect forms the cornerstone and motivation of OMA, i.e., searching for suitable and trustworthy methods that use the structure's vibration output to provide the best estimates of its in-situ physical properties. Knowledge of these in-situ properties is significant, for instance, in assessing changes in material properties relative to the nominal values stated at the construction era due to degradation processes and long-term effects. A key consequence of OMA is the development of damage-detection strategies to track the health state of a structure by periodically examining its dynamic behavior over time. Hence, for OMA, achieving sufficient understanding of the structure's dynamics and mechanics is key to capturing its real health state for SHM. A range of interdisciplinary challenges usually arises, including random-vibration aspects under linear or nonlinear regimes; treatment of service conditions that may be stationary or nonstationary; and expertise in analogue-to-digital acquisition and specialized signal-processing tools, often necessitating application-driven assumptions and customized simplifications [12]. The current chapter is dedicated specifically to conventional OMA approaches and the main goal is to deal with structural systems which can be defined as linear time-invariant (LTI) systems [13]. The underlying assumption concerns structures showing linear behavior (i.e., elastic), as is usually the case in operational in-service life, and having time-invariant parameters, namely, stationary conditions. In the SHM context of long-term continuous monitoring, material properties evolve so slowly over long periods that, within any single experimental dynamic

test, they may be considered essentially constant.

2.1 Historical and Theoretical Development of OMA

2.1.1 History of OMA

The field regarding vibrations of bodies goes back to ancient history; for instance, ancient Greek mathematicians and philosophers, most notably Pythagoras, studied sounds from strings of differing lengths, setting the origin of music and defining notes and octaves [12]. During the Renaissance, Galileo Galilei, in his celebrated Discourses Concerning Two New Sciences (1638), treated the vibration of bodies and described resonance in distant bodies with identical natural frequency, denoting it as sympathetic vibration [12]. In 1755, D. Bernoulli of Switzerland set out the groundwork for the modal superposition principle by observing that a vibrating string can be represented as a superposition of simple harmonics, the principle of coexistence" [12]. Probably, in the following centuries, every scientific and engineering field owe to Joseph Fourier, who developed his theorem when analyzing heat transmission principles in 1822. Referring to more recent eras, it is worth mentioning the British physicist J.W. Strutt, better known as the 3rd Baron Rayleigh, whose contributions over the last two centuries represent the basic framework of modern structural dynamics, including the definition of damping that accounts for both mass and stiffness quantities [12].

Rudimentary OMA can be linked to 19th-century damage detection on railway lines [14]; nevertheless, the principal pre-OMA discipline was experimental modal analysis (EMA) [13]. Two main branches are thus recognised within dynamic identification according to the monitored quantities: input–output and output-only [12]. EMA measures both the imposed input excitation and the resulting vibration response to characterise how the structure acts as a filter from input to output. Input–output EMA techniques are mainly associated with mechanical engineering and related vibration-control studies, since the typical system scale permits capturing both the input signal and the structural response. In mechanical engineering, early work centered on monitoring the condition of rotating machinery while it was running normally, rather than during start-up or shut-down [14]. Engineers typically used accelerometers, as well as velocity sensors and laser-based contactless displacement transducers, for this purpose. On the other hand, although OMA shares much of its theory with EMA, OMA designates output-only approaches that attempt to characterise the system using only the measured response. Hence, it is termed "operational," since it addresses the unmeasured random loads present during in-service operation. This proved decisive for OMA versus EMA in civil applications, as the large scale makes it infeasible to induce proper artificial excitation for the full dynamics and impractical to measure random inputs such as wind with precision.

As shown in Fig. 2.1, a standard basic assumption is formulated to describe the

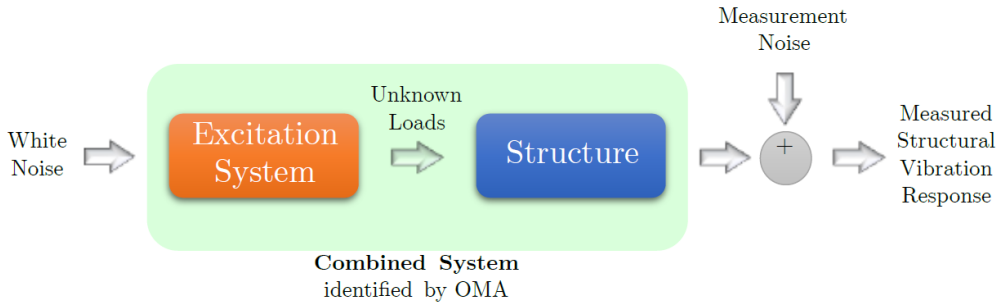

Figure 2.1: Combined system identified in the OMA framework.

nature of unknown inputs. One considers a white-noise input at the source, passed through a loading-excitation filter to produce the actual unknown random forces acting on the structure under operating conditions (e.g., wind, traffic), which yield the measured vibration response. This motivates the OMA concept of identifying the "whole system" (the combined system [13]), i.e., both the structural system and the loading-excitation system [12]. In civil applications, because acceleration responses are typically in the mg range, very sensitive, high-performance, low-noise piezoelectric accelerometers are needed [13]; also common are force-balance accelerometers and, thanks to micro-electronics advances, MEMS devices, along with electric-resistance and vibrating-wire strain gauges [14]. Thus, the primary distinction between EMA and OMA concerns the input. EMA uses a measured, known input, whereas in OMA the input is completely unknown [13]. OMA's widespread adoption over EMA can also be ascribed to the relatively low cost and speed of experiments, together with advances in computation [12]. For instance, one does not need to stop using the building, since it is desirable to capture responses under typical service conditions. Modern OMA became properly formalised at the beginning of the last century [13]; notable publications span the 1930s–1960s, especially for earthquake loading and ambient tests on buildings [12], with later growth supported by improved computing and the 1965 introduction of the FFT [15]. Nonetheless, from about the 1980s onward the theoretical basis was mature enough to enable practical implementations of vibration-based damage assessment systems in civil engineering [14]. In parallel national and international regulations introduced mandatory provisions for periodic or continuous health monitoring of strategic structures and infrastructures for public-safety purposes [14].

2.1.2 Signal processing basics for OMA

Generally, a signal is any function of several independent variables that has information about a physical system. Considering time as an independent variable, it is possible to distinguish between continuous-time signals, $x(t)$, and discrete-time ones, $x(t_k)$, being t_k a k-th time instant [15]. Another fundamental classification relies on the signal's amplitude (the dependent variable), which is that analog signals have both time and

amplitude as continuous variables, whereas numerical or digital signals have time and amplitude as discrete sequences. As noted earlier, the theory has roots in the 1600s, major advances in the 17th–18th centuries, and a revolution in the 1940s–1960s due to computing capabilities and new electronics and algorithms. Since then, physical quantities have been discretely sampled and stored in finite-precision computers, shifting the theoretical and mathematical background from continuous to discrete domains. Signal processing comprises transforming signals to express their intrinsic information in a more directly interpretable way [15].

Generally, a signal is any function of several independent variables that has information about a physical system. Considering time as an independent variable, it is possible to distinguish between continuous-time signals, $x(t)$, and discrete-time ones, $x(t_k)$, being t_k a k-th time instant [15]. Another fundamental classification relies on the signal's amplitude (the dependent variable), which is that analog signals have both time and amplitude as continuous variables, whereas numerical or digital signals have time and amplitude as discrete sequences. As noted earlier, the theory has roots in the 1600s, major advances in the 17th–18th centuries, and a revolution in the 1940s–1960s due to computing capabilities and new electronics/algorithms. Since then, physical quantities have been discretely sampled and stored in finite-precision computers, shifting the theoretical and mathematical background from continuous to discrete domains. Signal processing involves transforming signals to express their intrinsic information in a more directly interpretable way [15].

The Fourier theorem includes a fundamental starting point in signal processing, which permits the decomposition of an arbitrary signal into a linear combination of sinusoids at different frequencies (harmonics). Initially developed for periodic signals, it was generalized to non-periodic signals by letting the period be infinite. In continuous time, the direct and inverse Fourier transforms read [13]:

$$X(f) = \int_{-\infty}^{\infty} x(t) e^{-i2\pi ft} dt \quad ; \quad x(t) = \int_{-\infty}^{\infty} X(f) e^{i2\pi ft} df, \tag{2.1}$$

Here i is the imaginary unit, f denotes continuous frequency, and t indicates continuous time. The Fourier transforms exhibit a variety of properties such as linearity, time shift, integration and differentiation, and convolution properties [13]. The last one states that a time-domain convolution corresponds to mere multiplication in the Fourier frequency domain. Dealing with finite length $T = N\Delta t$ digital signals $x_n = x(n\Delta t)$ with $n = 0, ..., N-1$, sampled with a sampling frequency $f_s = 1/\Delta t$, being $\Delta t = t_{n+1} - t_n$ the sampling period, the discrete Fourier transform (DFT) and its inverse form have been formalized, considering a discrete frequency domain described by $f_k = k/T$ with $k = 0, ..., N-1$:

$$X_k = X(f_k) = \sum_{n=0}^{N-1} x_n e^{\frac{-i2\pi kn}{N}} \quad ; \quad x_n = \frac{1}{N} \sum_{k=0}^{N-1} X_k e^{\frac{i2\pi kn}{N}}. \tag{2.2}$$

In accordance with the Shannon-Nyquist theorem [13, 14], the maximum representable frequency in the discrete Fourier domain (the Nyquist frequency) is equal to half the sampling frequency:

$$f_{\max} = \frac{f_s}{2}. \tag{2.3}$$

In general, OMA measurements are viewed as a random (stochastic) process the set of all realizations of random variables over time. Such processes are described via probability density functions, mean, variance, auto- and cross-correlation functions, auto- and cross-spectral density functions, and coherence functions. Under the basic hypothesis of conventional OMA, signals are usually treated as stationary, stochastic, ergodic random processes. Stationarity implies that the properties that characterize the signals, e.g., mean μ_X and autocorrelation R_{XX} do not vary with time [13]. Periodic finite-length stationary stochastic process (finite-energy signals) implies the time-average statistic as a finite constant and obtainable via a discrete estimator over arbitrary sample sequences [14, 15], rather than by an ensemble-average expectation that presumes infinitely many realizations over time (infinite-energy signals) [15]. Hence, although random variables would in principle require a collection of signals covering all possible realizations at each time instant, if the observation window is infinitely long, a single digital signal suffices to estimate the characteristics of the entire random process:

$$\mu_X = \mathbb{E}[x(t_k)] = \lim_{N\to\infty} \frac{1}{N} \sum_{k=1}^{N} x(t_k), \tag{2.4}$$

$$R_{XX}(\tau) = \mathbb{E}[x(t_k)x(t_k+\tau)] = \lim_{N\to\infty} \frac{1}{N} \sum_{k=1}^{N} x(t_k)x(t_k+\tau). \tag{2.5}$$

Another key way to describe stationary stochastic processes over a set period T is by using power spectral density (PSD) functions. The two main types are the auto-PSD, which is a real-valued function, and the cross-PSD, which is a complex-valued function.[13]

$$S_{XX}(f) = \lim_{T\to\infty} \mathbb{E}\left[\frac{1}{T} X_k^* X_k\right] = \lim_{T\to\infty} \mathbb{E}\left[\frac{1}{T} \left|{X_k}^2\right|\right], \tag{2.6}$$

$$S_{YY}(f) = \lim_{T\to\infty} \mathbb{E}\left[\frac{1}{T} Y_k^* Y_k\right] = \lim_{T\to\infty} \mathbb{E}\left[\frac{1}{T} \left|Y_k\right|^2\right], \tag{2.7}$$

$$S_{XY}(f) = \lim_{T\to\infty} \mathbb{E}\left[\frac{1}{T} X_k^* Y_k\right], \tag{2.8}$$

typically, the one-sided version is used, which is formed by doubling the amplitude, but

preserving the phase:

$$G_{XX}(f) = 2S_{XX}(f), \tag{2.9}$$

$$G_{YY}(f) = 2S_{YY}(f), \tag{2.10}$$

$$G_{XY}(f) = 2S_{XY}(f). \tag{2.11}$$

It's important to remember that power spectral density (PSD) and correlation functions are actually related through the Fourier transform (known as the Wiener-Khinchin relations [13]). This means the PSD found by the Fourier transform of the correlation functions:

$$S_{XX}(f) = \int_{-\infty}^{+\infty} R_{XX}(\tau)e^{-i2\pi f\tau}d\tau, \tag{2.12}$$

$$S_{YY}(f) = \int_{-\infty}^{+\infty} R_{YY}(\tau)e^{-i2\pi f\tau}d\tau, \tag{2.13}$$

$$S_{XY}(f) = \int_{-\infty}^{+\infty} R_{XY}(\tau)e^{-i2\pi f\tau}d\tau. \tag{2.14}$$

The function $\gamma^2_{XY}(f)$ (coherence) is given by the ratio between the squared cross-PSD and the product of the auto-PSDs. It takes values in [0,1] and indicates the degree of linear dependence of two signals, which assists in detecting nonlinearities, being formally akin to the Pearson linear correlation coefficient [16]:

$$\gamma^2_{XY}(f) = \frac{|G_{XY}(f)|^2}{G_{XX}(f)G_{YY}(f)} = \frac{|S_{XY}(f)|^2}{S_{XX}(f)S_{YY}(f)} \tag{2.15}$$

Based on the Blackman-Tukey procedure [13], for finite and long enough stationary ergodic processes, it is possible to calculate the correlation function from a direct computation procedure.

$$\hat{R}_{XX}(r\Delta t) = \frac{1}{(N-r)\sigma^2_X}\sum_{n=1}^{N-r}(x_n - \mu_X)(x_{n+r} - \mu_X), \quad r = 0,1,...,m \tag{2.16}$$

According to the acknowledged Welch procedure, the introduction of the efficient Fast Fourier Transform (FFT) algorithm enabled a direct computation of the PSD [13]. Accuracy is improved by computing a one-sided PSD estimator that splits the signal into segments of duration T and averages the spectra from the Fourier transform of each segment. Because the Fourier transform assumes periodicity, applying the FFT to non-periodic segments introduces spectral inaccuracies. This leakage effect disperses the energy of every frequency line over a wider bandwidth. While it cannot be fully avoided, it can be mitigated by windowing, i.e., setting the signal to zero at the window's

boundaries.

$$w_{\text{rectangular}}(t_k) = \begin{cases} 1 & \text{if } 0 \leq t_k \leq T, \\ 0 & \text{otherwise.} \end{cases} \tag{2.17}$$

However it is preferred to adopt the Hanning or cosine window $w_{\text{hanning}}(t_k)$ which is characterized by a greater side-lobe reduction of 32 dB, but with a broader bandwidth dispersion

$$w_{\text{hanning}}(t_k) = \begin{cases} \sqrt{\frac{8}{3}} \left[\frac{1}{2} - \frac{1}{2}\cos\left(\frac{2\pi t}{T}\right)\right] & \text{if } 0 \leq t_k \leq T, \\ 0 & \text{otherwise.} \end{cases} \tag{2.18}$$

Windowing sometimes needs the introduction of some correction factor to adjust frequency spectra amplitude to maintain the signal's energy equivalence, as demonstrated by the $\sqrt{\frac{8}{3}}$ factor in Eq. (2.18) [13]. Beyond the Shannon-Nyquist theorem, a further key issue is aliasing; undersampling of frequencies above the Nyquist frequency can make them show up incorrectly within the measured band. The standard remedy is an anti-aliasing filter, an analog low-pass filter used before acquisition, to suppress those high-frequency components [13]. Owing to the finite transition band of real filters, the usable Nyquist frequency is commonly reduced by about 20%.

2.2 Conventional OMA stationary methods

2.2.1 Frequency domain methods

2.2.1.1 Peak-peaking method

The peak-peaking method, also known as the basic frequency-domain method, is among the earliest and simplest OMA algorithms developed, and is now mainly applied as a stand-alone tool for quick in-situ assessment of the preliminary effectiveness of ambient vibration testing [13]. It can be viewed as an SDOF method because it assumes each mode is identified separately, an assumption that seldom holds in reality. Therefore, it performs best for well-separated modes with low damping. In the spectral domain, an r-th mode is well-separated if the minimum distance from any other mode is greater than its bandwidth B, given by $B = 2\xi_r f_r$, with ξ_r the damping ratio and f_r the natural frequency [12]. The modal parameters are obtained locally, i.e., from the analysis of each sensor channel independently. Note that this method returns only the ODS, not the proper mode shapes. As its name suggests, it is based on identifying the peaks on the PSD matrix graph, which is characterized also by a certain degree of subjectivity, being the main drawback of this technique. When the r-th mode is dominant, the modal decomposition is simplified by considering only the r-th modal coordinate $p(t)$ and mode shape ϕ_r, i.e.

$$y(t) = \phi_r p(t). \tag{2.19}$$

The correlation function matrix of the output signal $R_{YY}(\tau)$ can be obtained by considering the autocorrelation of the modal coordinate $R_{p_r p_r}(\tau)$, i.e.

$$R_{YY}(\tau) = \mathbb{E}[y(t+\tau)y^T(t)] = R_{p_r p_r}(\tau)\phi_r\phi_r^T. \tag{2.20}$$

Using the Fourier transform, the one-side PSD matrix can be calculated by considering the spectral density of the modal coordinate $G_{p_r p_r}(f)$, i.e.

$$G_{YY}(f) = G_{p_r p_r}(f)\phi_r\phi_r^H. \tag{2.21}$$

From the latter equation, the PSD $G_{YY}(f) = [g_1, g_2...]$ of the response $y(t)$ is seen to contain the modal information of interest, where g_i denotes the generic PSD column vector. In addition, at the resonance frequency the system may be approximated as an SDOF system governed only by the r-th mode. Hence, the PSD matrix is rank 1, and any column or row is proportional to ϕ_r and may be taken as an estimate of it as

$$\hat{\phi_r} = g_i. \tag{2.22}$$

Commonly, for clearer discrimination of structural modes of real interest, the PSD is examined alongside the coherence function (Eq. (2.15)); when it approaches 1, it indicates a high SNR. Expressed typically in dB, the SNR quantifies how much unwanted noise contaminates the desired signal and is defined as the base-10 logarithm of the square ratio between A_y and A_n, i.e.

$$\text{SNR} = \log_{10}\left(\frac{A_y}{A_n}\right)^2. \tag{2.23}$$

Despite its simplicity, the peak-peaking method is not reliable if used stand-alone, and more reliable and systematic procedures have been developed accordingly.

2.2.1.2 Frequency domain decomposition

The Frequency domain decomposition (FDD) method generalizes the peak-peaking approach by overcoming the requirement of well-separated modes and by concentrating the evaluation in a single plot based on the SVD of the PSD matrix. In this framework, the response signal can be decomposed according to the modal decomposition, and the correlation function matrix $RYY(\tau)$ of the output signal is obtained by considering the autocorrelation matrix of the modal coordinates $RPP(\tau)$, i.e.

$$R_{YY}(\tau) = \mathbb{E}[y(t+\tau)y^T(t)] = \Phi R_{PP}(\tau)\Phi^T. \tag{2.24}$$

Using the Fourier transform pair property, the one-sided PSD matrix follows from the spectral density of the modal coordinate $GPP(f)$, i.e.

$$G_{YY}(f) = \Phi G_{PP}(f)\Phi^H. \tag{2.25}$$

The response PSD matrix can then be decomposed via singular value decomposition, a linear algebra tool that generalizes diagonalization [14]. The matrix $G_{YY}(f)$ is decomposed into a diagonal matrix $\Sigma = \text{diag}(\sigma_1, \sigma_2, ...)$ of singular values (SVs) sorted in descending order and two orthogonal/unitary matrices $U = [u_1, u_2, ...]$ and V, with $U^H U = UU^H = I$. Since the PSD is a positive definite Hermitian matrix, it holds that $U = V$, therefore:

$$G_{YY}(f) = U\Sigma V^H = U\Sigma U^H. \tag{2.26}$$

Comparing Eqs. (2.25)–(2.26) shows that $G_{PP}(f)$ is diagonal iff the modal coordinates are uncorrelated, so the SVs can be read as the auto spectral densities of the modal coordinates [12]. In that situation, one links the estimated output PSD to its SVD and reduces it to rank 1 at a chosen frequency f_k, i.e.

$$G_{YY}(f_r) = \sigma_r u_r(f_r) u_r^H(f_r). \tag{2.27}$$

and determines the number of mode shapes from the rank of the SV matrix (non-zero SVs), estimating each r-th mode shape from the left singular vectors U, i.e.

$$\hat{\phi_r} = u_r(f_r). \tag{2.28}$$

If the modal coordinates are not uncorrelated, the mode-shape estimates are biased and should not be used for physical interpretation [12]. In any case, FDD mode shapes are inherently biased, since SVD enforces orthogonality of singular vectors; thus [12] recommends using only the first singular vector at the dominant frequency line as the best estimate, i.e. impose σ_1 in Eq. (2.27). Because noise affects the peak of the first SV at a single f_k, EFDD augments FDD by exploiting information around peaks, extracting an SDOF "bell" from a band of SVs about the mode of interest. The retained band is set by correlating nearby mode-shape estimates via the Modal Assurance Criterion (MAC). For two mode shapes $\vec{\phi}_a$ and $\vec{\phi}_b$,

$$\text{MAC}(\phi_a, \phi_b) = \frac{|\phi_a|^H \phi_b{}^2}{\left(\phi_a{}^H \phi_a\right)\left(\phi_b{}^H \phi_b\right)} \quad , \quad 0 \leq \text{MAC}(\phi a, \phi b) \leq 1. \tag{2.29}$$

MAC equal 1 indicates perfect correlation, whereas 0 indicates none [18]. Hence, considering the peak estimate $\hat{\phi} r$ and nearby shapes, SVs are retained when MAC exceeds a threshold, typically 80%. The SDOF bell in the PSD is then mapped back to the time domain via the inverse transform; the resulting correlation function corresponds to a free decay of an SDOF system. Consequently, beyond natural frequency and mode

shape, EFDD permits estimating the damping ratio ξ_r for the r-th mode [12], e.g., via logarithmic decrement with a linear regression over zero-crossings or extremes of the free-decay correlation function [13, 17]. The damped natural frequency is

$$f_{r,d} = f_r\sqrt{1-\xi_r^2}. \tag{2.30}$$

For assisted and automatic selection of structural modal peaks (rather than noise) on the SVD of the PSD matrix, one may use the modal coherence indicator $d_1(f_k)$ [18], a correlation between the first singular vector at f_k and neighboring f:

$$d_1(f_k) = u_1^T(f)u_1(f_k). \tag{2.31}$$

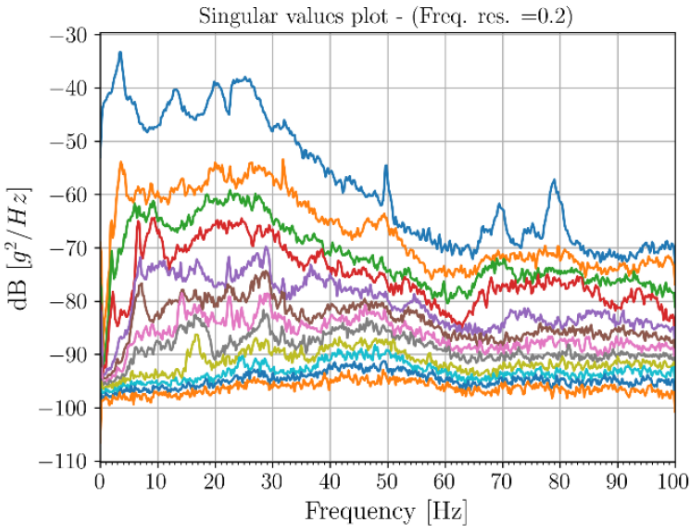

Figure 2.2: SVD graph of the PSD within the FDD method

Note also that FDD benefits from an built-in noise-separation capability due to the SVD tool. In the synthetic-data example, the SVD graph of the PSD matrix reveals a sinusoidal excitation, visible as constant peaks on the SV lines; ignoring these, the genuine peaks on the first SV correspond to the natural frequencies at 1.91 Hz, 3.57 Hz, and 6.63 Hz. Furthermore, without targeted noise at specific frequencies, the SV graph exposes the structural-mode peaks of interest, which increase significantly in amplitude, particularly in the first SV, above the noise floor.

2.2.2 Time domain methods

2.2.2.1 Stochastic state-space models

The time-domain dynamics of a structural system can be represented using a physically based parametric model, namely a state-space model [13]. The core idea is to rewrite the general second-order ODEs of motion, into two first-order ODEs denoted as state

and observation, by introducing the state vector $s(t)$:

$$s(t) = \begin{bmatrix} y(t) \\ \dot{y}(t) \end{bmatrix}. \tag{2.32}$$

The state variables are often termed hidden variables since they describe an internal (unmeasurable) model representation, while the real observed quantity for studying the system dynamics is the structural response. First, focusing on the continuous-time domain, where the drive vector is written as $f(t) = Pu(t)$. Input position matrix $P \in \mathbb{R}^{n \times N_{in}}$ and a function $u(t)$ have described the temporal change in the input actions, that n is the number of DOFs and N_{in} is the number of inputs. The specific form of these two terms P and $u(t)$ depends on the intrinsic nature of the input actions, i.e. on which DOFs the input is acting on. For instance, in earthquake engineering, the input is commonly represented by an acceleration ground input indicated as $\ddot{u}_g(t)$ acting only at the base DOFs of the structure. Nevertheless, it is reformulated as

$$M\ddot{y}(t) + C\dot{y}(t) + Ky(t) = P\ u(t), \tag{2.33}$$

The first derivatives of the state vector are

$$\dot{s}(t) = \begin{bmatrix} \dot{y}(t) \\ \ddot{y}(t) \end{bmatrix}, \tag{2.34}$$

The first component $\dot{s}_1(t)$ of Eq. (2.34) is directly given by

$$\dot{s}_2(t) = \begin{bmatrix} 0 & I \end{bmatrix} s(t) + \begin{bmatrix} 0 \end{bmatrix} u(t), \tag{2.35}$$

while the second component $\dot{s}_1(t)$ of Eq. (2.34) follows by making explicit the response acceleration in Eq. (2.33):

$$\dot{s}_2(t) = \begin{bmatrix} -M^{-1}K & -M^{-1}C \end{bmatrix} s(t) + \begin{bmatrix} -M^{-1} \end{bmatrix} Pu(t), \tag{2.36}$$

which yields the state equation

$$\begin{aligned} \dot{s}(t) &= \begin{bmatrix} 0 & I \\ -M^{-1}K & M^{-1}C \end{bmatrix} s(t) + \begin{bmatrix} 0 \\ -M^{-1} \end{bmatrix} Pu(t) \qquad \Leftrightarrow \\ \dot{s}(t) &= A_c s(t) + B_c u(t), \end{aligned} \tag{2.37}$$

in which $A_c \in \mathbb{R}^{2n \times 2n}$ is the state transition matrix, which transforms the current state into the next state representation, and $B_c \in \mathbb{R}^{2n \times n}$ is the input influence matrix, the subscript c denotes the continuous time domain. The observation equation depends on the number l and the type of sensors, which used to monitor the physical quantities

characterizing the response of the structure gathered in $y_l(t)$. Ideally, monitoring both accelerations, velocities, and displacements at all n DOFs, the response vector $y_l(t)$ belongs to $\mathbb{R}^{3n\times 1}$, gathering on the column dimensions the displacements $y(t)$, velocities $\dot{y}(t)$, and accelerations $\ddot{y}(t)$. It could be theoretically expressed as a function of the state vector, and decomposed through output location matrices C_a, C_v, and C_d belonging to $\mathbb{R}^{n\times n}$, i.e.

$$y_l(t) = C_a\ddot{y}(t) + C_v\dot{y}(t) + C_d y(t) \tag{2.38}$$

and substituting $\ddot{y}(t)$ from Eq. (2.33), it becomes

$$\tilde{y}_l(t) = \begin{bmatrix} C_d - C_aM^{-1}K & C_v - C_aM^{-1}C \end{bmatrix} \begin{bmatrix} y(t) \\ \dot{cy}(t) \end{bmatrix} + C_aM^{-1}Bu(t) \tag{2.39}$$

The last relation provides only the acceleration part of $y_l(t)$, hence $\tilde{y}_l(t)$. It also shows that, in the state-space formulation, acceleration measurements in the observation equations depend explicitly on the state variables (displacements and velocities). Contrarily, displacement and velocity measurements are directly provided by the state variables and may be affected only by direct input. Therefore, considering a plausible and general scenario in which, for every single DOF, both displacements, velocities, and accelerations are measured, observation equations which express response vector $y_l(t)$ in Eq. (2.38) as a function of state variables $s(t)$ becomes

$$\begin{aligned} y_l(t) &= \begin{bmatrix} C_d & 0 \\ 0 & C_v \\ C_d - C_aM^{-1}K & C_v - C_aM^{-1}C \end{bmatrix} s(t) + \begin{bmatrix} 0 \\ 0 \\ C_aM^{-1} \end{bmatrix} Pu(t) \qquad \Leftrightarrow \\ y_l(t) &= C_c s(t) + D_c u(t), \end{aligned} \tag{2.40}$$

In last equation, $C_c \in \mathbb{R}^{3n\times 2n}$ is called the output influence matrix. $D_c \in \mathbb{R}^{3n\times 2n}$ is the direct transmission matrix and explains how an input directly reflects in the output response. Within the present structural-dynamics formulation, the input directly affects acceleration measurements. Besides the general formulation, in a practical SHM configuration where only accelerometer sensors are used on the structure, the observation model is restricted to Eq. (2.39), with a consequent reformulation of C_c and D_c.

All the previous mathematical elaborations permitted to rewriting of the motion equation according to the deterministic continuous-time state-space model according to the state equation and observation equation respectively, i.e.

$$\dot{s}(t) = A_c s(t) + B_c u(t)\,, \tag{2.41}$$

$$y_l(t) = C_c s(t) + D_c u(t). \tag{2.42}$$

The model is called deterministic since the excitation is considered deterministic, and

the modal information of the structural system resides in the eigenvalues of A_c. An infinite family of equivalent state-space models (realizations) exists for the same system. Applying a similarity transform with a non-singular square matrix T changes the realization but preserves the eigenvalues, and thus the modal content. Accordingly, in vibration experiments, the measured response is used to identify one realization among the infinitely many. For the discrete time-domain, with $t_r = r \cdot \Delta t$ (sampling period Δt), $r \in \mathbb{N}$, discrete state $s_r(t_r) = s(r \cdot \Delta t)$ of order n, under zero-order hold on the input and with N samples of l channels $y_r \in \mathbb{R}^l$, the discrete deterministic state-space form is obtained.

$$s_{r+1}(t_{r+1}) = As_r(t_r) + Bu_r(t_r)\,, \tag{2.43}$$

$$y_r(t_r) = Cs_r(t_r) + Du_r(t_r), \tag{2.44}$$

in which the state space matrices are defined as

$$A = e^{A_c \Delta t}\,, \tag{2.45}$$

$$B = (A - I)A_c^{-1}B_c\,, \tag{2.46}$$

$$C = C_c\,, \tag{2.47}$$

$$D = D_c. \tag{2.48}$$

To account for unmeasurable noise sequences, two random processes are introduced. The process noise w_r covers disturbances and modeling errors arising from inaccuracies of the state-space model in capturing the true system dynamics. The measurement noise v_r instead stems from sensor electronics, which convert physical analogue signals into finite-arithmetic, finite-memory digital data. These two noise processes are treated as additive components, as already indicated by the measurement-noise process in Fig. 2.1, and are assumed zero-mean Gaussian white noise, hence fully specified by second-order statistics. Therefore, for any pair of time instants p and q, the variance is given by

$$\mathbb{E}\left[\begin{pmatrix} w_p \\ v_p \end{pmatrix}\begin{pmatrix} w_q & v_q \end{pmatrix}\right] = \begin{cases} \begin{bmatrix} Q^{ww} & S^{wv} \\ (S^{wv})^T & R^{vv} \end{bmatrix} & \text{if } p = q \\ 0 & \text{if } p \neq q, \end{cases} \tag{2.49}$$

The matrices $Q^{ww} \in \mathbb{R}^{n\times n}$, $S^{wv} \in \mathbb{R}^{n\times l}$, and $R^{vv} \in \mathbb{R}^{l\times l}$ are the covariance matrices associated with the noise processes w_r and v_r [19]. Therefore, omitting the explicit dependence on discrete-time instants, the discrete-time deterministic (input) stochastic state-space model is given by

$$s_{r+1} = As_r + Bu_r + w_r\,, \tag{2.50}$$

$$y_r = Cs_r + Du_r + v_r, \tag{2.51}$$

In the context of OMA, since the input excitation is unknown and modeled as Gaussian white noise, a pure stochastic state space model can be defined by folding the unmeasurable input into the process and measurement noise sequences, i.e.

$$s_{r+1} = As_r + w_r\,, \tag{2.52}$$

$$y_r = Cs_r + v_r, \tag{2.53}$$

With this, the process noise directly plays the role of the unmeasurable input excitation, whereas the measurement noise is a direct disturbance visible in the measured output. Accordingly, the measured response separates into an observable system part and an unobservable direct disturbance, consistent with the combined-system concept (see Fig. 2.1). This is likewise manifested in the eigenvalues of the state matrix, which include poles from both the structural system and the input noise excitation process. Therefore, using stochastic state space time-domain parametric models in OMA, the key task is to find at least one realization of $A \in \mathbb{R}^{n\times n}$ and $C \in \mathbb{R}^{l\times n}$ to extract the modal information of interest. The matrices A and C are taken to be observable, implying all modes are observable in y_r [19]. Moreover, the system order n is still unknown and must be selected within the OMA procedure, with the requirement that the second-order statistics of the model output and the measured output coincide [19].

2.2.2.2 Covariance-equivalent representation of stochastic state space model

In agreement with the OMA framework, the stochastic state space model system's response is represented by a zero-mean Gaussian process, and thus the output covariance conveys all significant information to describe this random process. Hence, it is possible to define a covariance equivalent model as an estimated state space model characterized by an optimal unbiased estimator, i.e. the correct output covariance able to describe the statistical properties of the output process [13]. Assuming an LTI stationary stochastic process, the state vector is also a zero-mean Gaussian process characterized by the following state covariance matrix Σ_{s_r} which is independent of the time and uncorrelated with noise processes [19]:

$$\Sigma_{s_r} = \mathbb{E}\left[s_r s_r^T\right] \quad , \quad \mathbb{E}\left[s_r w_r^T\right] = \mathbb{E}\left[s_r v_r^T\right] = 0. \tag{2.54}$$

The Lyapunov equation provides an alternative definition for the state covariance matrix Σ_{s_r} considering the next state s_{k+1} [19]

$$\begin{aligned}\Sigma_{s_r} &= \mathbb{E}\left[s_{k+1} s_{k+1}^T\right] = \mathbb{E}\left[\left(As_k + w_r\right)\left(As_k + w_r\right)^T\right] \\ &= A\mathbb{E}\left[s_r s_r^T\right] A^T + \mathbb{E}\left[w_r w_r^T\right] \\ &= A\Sigma_{s_r} A^T + Q^{ww}.\end{aligned} \tag{2.55}$$

The output covariance matrix, i.e. the cross-correlation matrix of the measured output response from all sensors' channels for sample r and with finite time lag i, is defined in general as

$$R_i = \mathbb{E}\left[y_{r+i} y_r^T\right] \tag{2.56}$$

from which it is possible to derive the initial output covariance matrix R_0 for lag $i = 0$,

$$\begin{aligned} R_0 = \mathbb{E}\left[y_r y_r^T\right] &= \mathbb{E}\left[\left(Cs_k + v_r\right)\left(Cs_k + v_r\right)^T\right] \\ &= C\mathbb{E}\left[s_r s_r^T\right] C^T + \mathbb{E}\left[v_r v_r^T\right] \\ &= C\Sigma_{s_r} C^T + R^{vv}. \end{aligned} \tag{2.57}$$

It is possible to define the next state-output covariance matrix G which represents the covariance between the response of the system y_r and the updated state vector s_{r+1}

$$\begin{aligned} G = \mathbb{E}\left[s_{r+1} y_r^T\right] &= \mathbb{E}\left[\left(As_k + w_r\right)\left(Cs_k + v_r\right)^T\right] \\ &= A\mathbb{E}\left[s_r s_r^T\right] C^T + \mathbb{E}\left[w_r v_r^T\right] \\ &= A\Sigma_{s_r} C^T + S^{wv}. \end{aligned} \tag{2.58}$$

from which it is possible to obtain an alternative definition for the output covariance matrix sequence R_i, so that

$$R_i = CA^{i-1}G \quad , \quad R_{-i} = G^T\left(A^{i-1}\right)^T C^T. \tag{2.59}$$

The Eq. (2.59) has fundamental consequences which are at the base of stochastic subspace identification algorithms, being that output covariance can be considered as Markov parameters of an LTI system defined by state space matrices A, C, G, and R_0. In general, Markov parameters describe the input-output relationship of a discrete-time model with sampled response according to a pulse response function to a unit pulse input [24]. Therefore, R_i is directly estimable from the data (via G), and decomposing the sequence yields the state matrix A, whose poles constitute the solution sought in covariance-driven, stochastic state-space, time-domain identification.

2.2.2.3 Covariance-based stochastic-subspace identification

Over the past decades, OMA has seen the development of several time-domain techniques founded on correlation analysis of output vibration responses under natural excitation, which gradually supplanted forced-vibration tests. These output-only approaches are termed Natural Excitation Techniques (NExT); three well-known methods are the least squares complex exponential (LSCE), the Ibrahim time domain (ITD), and the eigenvalue realization algorithm (ERA), the last being closely akin to subspace identification. For LSCE, ITD, and ERA see [20, 21, 22]. Despite early popularity, NExT procedures were progressively set aside due to various limitations [13], and

stochastic subspace identification became preferred. The covariance-driven stochastic subspace identification (SSI-cov) is a parametric, time-domain algorithm derived from the Ho–Kalman realization scheme [23], producing state realizations from output-only measurements. SSI-cov uses the stochastic state-space model in Eqs. (2.52)-(2.53), with model order n, l measured DOFs, and N_d total output samples, where $s_r \in \mathbb{R}^n$, $y_r \in \mathbb{R}^l$, $A \in \mathbb{R}^{n\times n}$, and $C \in \mathbb{R}^{l\times n}$, under the assumption that all system states are controllable and observable. A state is controllable if reachable from any initial condition by suitable control; observable if determined completely from the input and output at a given time. In line with Eq. (2.16), the output correlation matrices $\hat{R}i \in \mathbb{R}^{l\times l}$ are computed with a user-defined finite lag $i \in \mathbb{N}$ (time shift / number of block rows) [13], i.e.

$$\hat{R}_i = \frac{1}{N_d - i} Y_{1:N_d-i} Y_{i:N_d}^T, \tag{2.60}$$

Matrices $Y_{1:N_d-i} = \begin{bmatrix} y_0 & y_1 & \dots & y_{N_d-i} \end{bmatrix}^T \in \mathbb{R}^{l\times N_d}$ and $Y_{i:N_d} \in \mathbb{R}^{N_d\times l}$ indicate the output measurements' time histories from l sensors, collected and rearranged. All correlation estimates assuming the role of output covariance matrices in SSI-cov are computed for lags i through $2i-1$ and assembled into a block Toeplitz matrix $T1|i \in \mathbb{R}^{il\times il}$ (a matrix with constant diagonals) as follows:

$$T_{1|i} = \begin{bmatrix} R_i & R_{i-1} & \dots & R_2 & R_1 \\ R_{i+1} & R_i & \ddots & \ddots & R_2 \\ \vdots & \ddots & \ddots & \ddots & \vdots \\ \vdots & \ddots & \ddots & \ddots & R_{i-1} \\ R_{2i-1} & R_{2i-2} & \dots & R_{i+1} & R_i \end{bmatrix}. \tag{2.61}$$

The subscript in $T_{1|i}$ indicates the indices of the first column of the matrix [19]. Using the Toeplitz matrix of output covariance matrices can reduce computational effort during modal identification, thereby improving the efficiency of the elaboration. For a system of order n, the choice of the block-rows parameter i must satisfy [13]

$$li \geq n. \tag{2.62}$$

The true order n of the state-space model is unknown. The Ho–Kalman algorithm is based on minimal realization, so it seeks the smallest n that guarantees full controllability and observability. Still, at the beginning of SSI-cov one may obtain a rough estimate of n by examining the rank of the output PSD or the SVD of the PSD (cf. FDD). This preliminary estimate guides the selection of the time-shift parameter to satisfy $i \geq n/l$. When the system is fully controllable and observable, the Toeplitz matrix admits the factorization into an observability matrix $O_i \in \mathbb{R}^{li\times n}$ (depending only on A and C) and a reversed controllability matrix $\Gamma_i \in \mathbb{R}^{n\times li}$ (depending only on

A and the next-state output covariance G), i.e.

$$T_{1|i} = \begin{bmatrix} C \\ CA \\ \vdots \\ CA^{i-1} \end{bmatrix} \begin{bmatrix} A^{i-1}G & \dots & AG & G \end{bmatrix} = O_i \Gamma_i. \tag{2.63}$$

Accordingly, matrix C can be taken directly from the first l rows of O_i, while matrix G is obtained from the last l columns of Γi. To obtain O_i and Γi separately, perform the SVD of the Toeplitz matrix:

$$T_{1|i} = U\Sigma V^T = \begin{bmatrix} U_1 & U_2 \end{bmatrix} \begin{bmatrix} \Sigma_1 & 0 \\ 0 & 0 \end{bmatrix} \begin{bmatrix} V_1 \\ V_2 \end{bmatrix} \approx U_1 \Sigma_1 V_1^T \tag{2.64}$$

where Σ is truncated to rank n (keeping $\Sigma_1 \in \mathbb{R}^{n\times n}$) and $U_1 \in \mathbb{R}^{li\times n}$, $V1^T \in \mathbb{R}^{n\times li}$. Consequently,

$$T_{1|i} = U_1 \Sigma_1 V_1^T = U_1 \left(\Sigma_1^{1/2}\Sigma_1^{1/2}\right) V_1^T = \left(U_1 \Sigma_1^{1/2}\right)\left(\Sigma_1^{1/2} V_1^T\right) = O_i \Gamma_i \,, \tag{2.65}$$

$$O_i = U_1 \Sigma_1^{1/2} T \,, \tag{2.66}$$

$$\Gamma_i = T^{-1} \Sigma_1^{1/2} V_1^T \,, \tag{2.67}$$

including a non-singular similarity matrix T since only one realization is identified among the equivalent ones; often one sets $T = I$. Having O_i and Γ_i, the next SSI-cov step estimates A and, together with C, yields the modal parameters. Recall C is read from the first l rows of O_i, and G from the last l columns of Γ_i. Two principal procedures for A are reported [13]. The first (NExT–ERA) builds the one-lag Toeplitz matrix $T_{2|i+1}$ of output covariances and exploits its factorization:

$$T_{2|i+1} = \begin{bmatrix} R_{i+1} & R_i & \dots & R_3 & R_2 \\ R_{i+2} & R_{i+1} & \ddots & \ddots & R_3 \\ \vdots & \ddots & \ddots & \ddots & \vdots \\ \vdots & \ddots & \ddots & \ddots & R_{i-1} \\ R_{2i} & R_{2i-1} & \dots & R_{i+2} & R_{i+1} \end{bmatrix} = O_i A \Gamma_i. \tag{2.68}$$

Thus, by taking into consideration equations (2.66)-(2.67) derived from SVD decomposition of the original output covariance Toeplitz matrix Eq. (2.61), the state matrix A estimate is given by

$$A = O_i^{\dagger} T_{2|i+1} \Gamma_i^{\dagger} = \left(\Sigma_1^{-1/2} U_1^T\right) T_{2|i+1} \left(V_1 \Sigma_1^{-1/2}\right). \tag{2.69}$$

where † denotes the Moore–Penrose pseudo-inverse [13]. The second approach to estimate A, due to Yi and Yun [25, 13], pre- and post-multiplies (2.61) by invertible matrices W_1 and W_2 (i.e., $W_1 T_{1|i} W_2$) and, after SVD, yields an alternative observability matrix:

$$O_i = W_1^{-1} U_1 \Sigma_1^{1/2} T. \tag{2.70}$$

Two weighting schemes are common: balanced realization (BR) and canonical variate analysis (CVA) [26]. In BR, choosing $W_1 = W_2 = I$ implies $O_i^T O_i = \Gamma_i \Gamma_i^T = \Sigma_1$ (Gram matrices); "balanced" indicates that input excitation transfers to the state and the state to the output in a comparable manner [13]. Using the shift-invariance property of O_i [27], further decompose O_i to make A explicit by defining $O_i^{\uparrow}$ (remove the last l rows of O_i) and $O_i^{\downarrow}$ (remove the first l rows) [28, 29], i.e.

$$O_i = \begin{bmatrix} C \\ CA \\ \vdots \\ CA^{i-1} \end{bmatrix} = \begin{bmatrix} O_i^{\uparrow} \\ CA^{i-1} \end{bmatrix} = \begin{bmatrix} C \\ O_i^{\downarrow} \end{bmatrix} \;\Rightarrow\; O_i^{\uparrow} = \begin{bmatrix} C \\ CA \\ \vdots \\ CA^{i-2} \end{bmatrix}, O_i^{\downarrow} = \begin{bmatrix} CA \\ CA^2 \\ \vdots \\ CA^{i-1} \end{bmatrix} \tag{2.71}$$

$$\Rightarrow \quad O_i^{\uparrow} A = O_i^{\downarrow} \quad \Rightarrow \quad A = {O_i^{\uparrow}}^{\dagger} O_i^{\downarrow} \tag{2.72}$$

On the other hand, the CVA weighting aims to balance the energy content across all system modes and retrieves the weighting matrices via Cholesky decompositions of two modified Toeplitz matrices [26]. $W1$ is defined as the inverse of the lower-triangular factor $[L^+]^{-1}$ obtained from the Cholesky factorization of a reversed one-time-lag Toeplitz matrix $T^+_{0|i-1}$, where the upper triangle is transposed, i.e.

$$T_{0|i-1} = \begin{bmatrix} R_0 & R_1^T & \dots & R_{i-2}^T & R_{i-1}^T \\ R_1 & R_0 & \ddots & \ddots & R_{i-2}^T \\ \vdots & \ddots & \ddots & \ddots & \vdots \\ \vdots & \ddots & \ddots & \ddots & {R_{i-1}}^T \\ R_{i-1} & R_{i-2} & \dots & R_1 & R_0 \end{bmatrix} = L^+ [L^+]^T \quad \Rightarrow \quad W_1 = [L^+]^{-1}. \tag{2.73}$$

Conversely, $W2$ is defined as the inverse of the lower-triangular factor $[L^-]^{-1}$ obtained from the Cholesky factorization of the reversed one-time-lag Toeplitz matrix of

output covariances $T^{-}_{0|i-1}$, where the lower triangle is transposed, i.e.

$$T_{0|i-1} = \begin{bmatrix} R_0 & R_1 & \dots & R_{i-2} & R_{i-1} \\ R_1^T & R_0 & \ddots & \ddots & R_{i-2} \\ \vdots & \ddots & \ddots & \ddots & \vdots \\ \vdots & \ddots & \ddots & \ddots & R_{i-1} \\ R_{i-1}^T & R_{i-2}^T & \dots & R_1^T & R_0 \end{bmatrix} = L^{-}[L^{-}]^T \quad \Rightarrow \quad W_2 = [L^{-}]^{-1}. \tag{2.74}$$

Accordingly, the eigenvalues of the weighted Toeplitz matrix in Eq. (2.61), i.e. $W_1 T_{1|i} W_2$, admit a geometric interpretation as canonical angles between two subspaces, ensuring balanced energy levels among all system modes [13, 26]. The OMA identification outcome is the desired modal parameter estimates (natural frequencies, damping ratios, and mode shapes) is obtained once the state matrix A and the output influence matrix C are identified. The eigenvalue decomposition (EVD) of matrix A leads to the diagonal matrix $\Lambda = \text{diag}([\lambda_1, ..., \lambda_u, ...\lambda_m]) \in \mathbb{R}^{n \times n}$ of discrete-time complex conjugate system poles pairs λ_u, λ_u^* (two-quadrant symmetry) and corresponding right eigenvectors ψ_u:

$$A = \Psi \Lambda \Psi^{-1} \quad , \quad A\psi_u = \lambda_u \psi_u, \tag{2.75}$$

where $1 \leq u \leq m$, with $m = n/2$ the number of eigenvalues of actual interest. This follows from retaining only modes with positive damping (positive imaginary parts) among the n complex-conjugate poles, so physically the modes of interest amount to half the system order [13, 30]. Undamped/damped natural frequencies and damping ratios are then computed by mapping from the Z-domain (discrete time) back to the Laplace domain (continuous time):

$$s_u = \frac{\ln(\lambda_u)}{\Delta t} \quad , \quad f_u = \frac{|s_u|}{2\pi} \quad , \quad \xi_u = -100 \frac{\mathfrak{Re}(s_u)}{|s_u|},$$

where s_u are the continuous-time poles, Δt is the sampling interval, $|\cdot|$ denotes the complex modulus, and $\mathfrak{Re}(s_u)$ the real part. Finally, the real part of the eigenvectors ψ_u provides the experimental mode shapes ϕ_u:

$$\phi_u = \mathfrak{Re}(\mathbf{C}\psi_u), \tag{2.76}$$

with $\Phi = [\phi_1, ..., \phi_u, ..., \phi_m] \in \mathbb{R}^{l \times m}$. It is worth noting that the entire SSI-cov procedure can equivalently be carried out using a block-Hankel matrix (with constant anti-diagonals) of the output-measurement covariance estimates in place of the Toeplitz matrix in Eq. (2.61). Moreover, the whole theoretical framework rests on estimated quantities (e.g., output covariances in Eq. (2.60)), since only a finite amount of data is available. Together with additive noise due to state-space modeling inaccuracies, sensor hardware noise, and computational noise from finite-precision arithmetic, the

rank of the estimated Toeplitz matrix cannot exactly reveal the true theoretical system order, also because the Toeplitz factorization is not mathematically exact in the presence of noise. In principle, the rank can be hinted at by the largest relative gap in the singular values (SVs) sorted in descending order. Nevertheless, in OMA the practical objective is reliable modal-parameter estimation rather than an exquisitely accurate dynamical description via a state-space model; hence a conservative overestimation of the system order is commonly adopted, leading to the well-known stabilization diagram (SD) approach [13]. In practice, the order n is started small and progressively increased to higher, over-specified values up to a user-defined limit. Accordingly, the Toeplitz output-covariance matrix is first sized to low dimensions and, following SSI-cov, poles are computed; the procedure is then repeated for successively larger matrix sizes. Recalling that in subspace identification only half the system order yields poles of interest (those with positive imaginary part), the model order grows by twos. Over-specifying n reveals spurious poles alongside the physical ones: "noise poles" when they are tied to the excitation system identified together with the structural system (combined-system concept, Fig. 2.1), and "mathematical modes" when they arise from the aforementioned inaccuracies and noise sources. As illustrated in Fig. 2.3, the stabilization diagram is a 2D plot showing, for each model order (ordinate), the poles versus natural frequency (abscissa). The SD affords a clear separation between stable physical modes and unstable spurious ones by tracking alignments of stable poles as the order increases. Stability checks discriminate stable from unstable poles in terms of frequency, damping ratio, and mode shapes, and are grouped into two classes: hard validation criteria (HVC), grounded in strict physical principles and applied to individual poles, and soft validation criteria (SVC), which set relative thresholds between pole pairs at two different orders [31, 32]. Under HVC, spurious poles include those lacking complex-conjugate pairing, modes with natural frequencies above the Nyquist frequency (accounting for any decimation), and poles with negative or excessively large positive damping ratios (typically limited to 10%) [31]:

$$\xi_u \leq 0.1, \tag{2.77}$$

$$f_u \leq \frac{f_s}{2}. \tag{2.78}$$

Assume pole a is identified at model order n. The SVC classify spurious poles by comparing a with any pole b at model orders $2, 4, \ldots, n/2$ using the following relative stability checks [13]:

$$\Delta\xi = \frac{\xi_a - \xi_b}{\xi_a} \leq 0.05, \tag{2.79}$$

$$\Delta f = \frac{f_a - f_b}{f_a} \leq 0.01, \tag{2.80}$$

$$1 - \mathrm{MAC}(\phi_a, \phi_b) \leq 0.02. \tag{2.81}$$

In general, the stabilization diagram can be adapted to any parametric OMA method. This graphical tool offers a clear separation between physical modes and spurious ones. Moreover the SD is often combined with at least the first SV curve of the PSD matrix to double-check that stable pole alignments coincide with the peaks of the PSD SV lines identified via FDD.

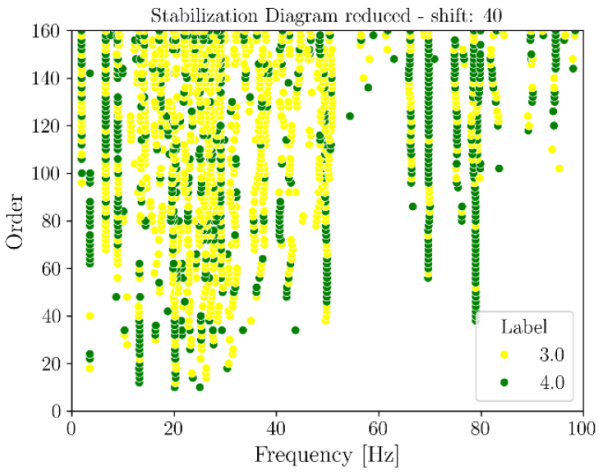

Figure 2.3: Stabilization diagram. The colors of the poles, identified by the numbers 0.0 to 4.0 in the legend, indicate respectively: unstable, stable in frequency, stable in frequency and mode shape, stable in frequency and damping, stable in frequency damping and mode shape.

2.2.2.4 Data-driven-based stochastic-subspace identification

The Data-driven SSI (SSI-dat) relies on the Kalman filter formulation of stochastic state-space modeling. SSI-dat begins by rearranging the measurements from l sensors collected as vectors $y_r \in \mathbb{R}^l$ at each time instant $r = 0, 1, ..., N_t$ into a Hankel matrix (with constant anti-diagonals) $Y_{0|2i-1}$ with a predefined number of block-rows set by the integer time-lag parameter i. Thus, the Hankel matrix has $2li$ block rows, and with

$N_d = N_t + 1$ total samples, the number of columns is $j = N_d - 2i + 1$:

$$Y_{0|2i-1} = \frac{1}{\sqrt{j}} \left[\begin{array}{cccccc} y_0 & y_1 & y_2 & \cdots & \cdots & y_{N_t-2i+1} \\ y_1 & y_2 & y_3 & \ddots & \ddots & y_{N_t-2i+2} \\ y_2 & y_3 & \ddots & \ddots & \ddots & y_{N_t-2i+3} \\ \vdots & \ddots & \ddots & \ddots & \ddots & \vdots \\ \vdots & \ddots & \ddots & \ddots & \ddots & y_{N_t-i-1} \\ y_{i-1} & y_i & \ddots & \ddots & \ddots & y_{N_t-i} \\ \hline y_i & y_{i+1} & \ddots & \ddots & \ddots & y_{N_t-i+1} \\ y_{i+1} & y_{i+2} & \ddots & \ddots & \ddots & y_{N_t-i+2} \\ \vdots & \ddots & \ddots & \ddots & \ddots & \vdots \\ y_{2i-2} & y_{2i-1} & \ddots & \ddots & \ddots & y_{N_t-1} \\ y_{2i-1} & y_{2i} & \cdots & \cdots & y_{N_t-1} & y_{N_t} \end{array}\right] = \left[\begin{array}{c} Y_p \\ \hline Y_f \end{array}\right]. \tag{2.82}$$

The Hankel matrix can be partitioned into two submatrices, the past data matrix Y_p and the future data matrix Y_f, each of size $li \times j$. Within the SSI-data framework, the Kalman state vectors sr (obtained from output observations up to time $r-1$) are collected into the Kalman state-sequence matrix $S_i = [s_i, s_{i+1}, ..., s_{i+j-1}]$ [13, 19]. This matrix is estimated as $\hat{S}_i$ by orthogonally projecting the row space of the future data matrix Y_f onto the row space of the past data matrix Y_p, via the projection matrix Π_i:

$$\Pi_i = Y_f / \underline{Y_p} = Y_f Y_p^T \left(Y_p Y_p^T\right)^\dagger Y_p, \tag{2.83}$$

where the underline $\underline{Y_p}$ indicates that the projection result lies in the row space of the past data matrix. Note that $Y_f Y_p^T$ contains the output autocorrelation used to form the Toeplitz matrix in SSI-cov, revealing the tight link between this orthogonal projection and output covariances. Assuming full controllability and observability [13], and provided that i satisfies Eq. (2.62), the main theorem of stochastic subspace identification states that Π_i factors into the extended observability matrix O_i and the Kalman-filter state sequence $\hat{S}_i$ [19], i.e.

$$\Pi_i = O_i \hat{S}_i = \begin{bmatrix} C \\ CA \\ \vdots \\ CA^{i-1} \end{bmatrix} \begin{bmatrix} \hat{s}_i & \hat{s}_{i+1} & ... & \hat{s}_{i+j-1} \end{bmatrix}. \tag{2.84}$$

The Hankel matrix of output data can be factorized by the linear-algebra LQ decomposition, yielding a lower triangular matrix L and an orthogonal matrix Q

($QQ^T = Q^TQ = I$). Owing to the block-row structure of the output-data Hankel matrix, the lower triangular factor can be partitioned into blocks with $L11 \in \mathbb{R}^{li \times li}$, $L21 \in \mathbb{R}^{l \times li}$, $L22 \in \mathbb{R}^{l \times l}$, $L31 \in \mathbb{R}^{l(i-1) \times li}$, $L32 \in \mathbb{R}^{l(i-1) \times l}$, and $L33 \in \mathbb{R}^{l(i-1) \times l(i-1)}$. Consequently, the orthogonal factor is likewise decomposed as $Q1 \in \mathbb{R}^{j \times li}$, $Q2 \in \mathbb{R}^{j \times l}$, and $Q_3 \in \mathbb{R}^{j \times l(i-1)}$, so that

$$Y_{0|2i-1} = LQ = \begin{bmatrix} L_{11} & 0 & 0 \\ L_{21} & L_{22} & 0 \\ L_{31} & L_{32} & L_{33} \end{bmatrix} \begin{bmatrix} Q_1^T \\ Q_2^T \\ Q_3^T \end{bmatrix}. \tag{2.85}$$

As a result, the projection matrix can be numerically obtained directly from the LQ decomposition of the output data Hankel matrix as follows

$$\Pi_i = Y_f / \underline{Y_p} = \begin{bmatrix} L_{21} \\ L_{31} \end{bmatrix} \begin{bmatrix} Q_1^T \end{bmatrix}. \tag{2.86}$$

Using Eq. (2.84) it is possible to obtain the extended observability matrix O_i and the Kalman filter state sequence matrix $\hat{S}_i$ using the SVD of the numerically estimated projection matrix (2.86), which resembles in some way the decomposition of the SSI-cov Toeplitz matrix (refer to Eq. (2.64)):

$$\Pi_i = U\Sigma V^T = \begin{bmatrix} U_1 & U_2 \end{bmatrix} \begin{bmatrix} \Sigma_1 & 0 \\ 0 & 0 \end{bmatrix} \begin{bmatrix} V_1 \\ V_2 \end{bmatrix} \approx U_1 \Sigma_1 V_1^T, \tag{2.87}$$

so obtaining

$$O_i = U_1 \Sigma_1^{1/2} T, \tag{2.88}$$

$$\hat{S}_i = O_i^{\dagger} \Pi_i, \tag{2.89}$$

where T is a transformation matrix which can be considered as an identity matrix. Now it is feasible to calculate the state matrices A and C to get the modal parameter of interest.

Alternatively, the output data Hankel matrix can be decomposed considering the following rearrangement with past output matrix with a block row added Y_p^+ and future

matrix with first block row removed Y_f^-:

$$Y_{0|2i-1} = \frac{1}{\sqrt{j}} \left[\begin{array}{cccccc} y_0 & y_1 & y_2 & \cdots & \cdots & y_{N_t-2i+1} \\ y_1 & y_2 & y_3 & \ddots & \ddots & y_{N_t-2i+2} \\ y_2 & y_3 & \ddots & \ddots & \ddots & y_{N_t-2i+3} \\ \vdots & \ddots & \ddots & \ddots & \ddots & \vdots \\ \vdots & \ddots & \ddots & \ddots & \ddots & y_{N_t-i-1} \\ y_{i-1} & y_i & \ddots & \ddots & \ddots & y_{N_t-i} \\ \hline y_i & y_{i+1} & \ddots & \ddots & \ddots & y_{N_t-i+1} \\ \hline y_{i+1} & y_{i+2} & \ddots & \ddots & \ddots & y_{N_t-i+2} \\ \vdots & \ddots & \ddots & \ddots & \ddots & \vdots \\ y_{2i-2} & y_{2i-1} & \ddots & \ddots & \ddots & y_{N_t-1} \\ y_{2i-1} & y_{2i} & \cdots & \cdots & y_{N_t-1} & y_{N_t} \end{array}\right] = \left[\begin{array}{c} Y_{0|i-1} \\ \hline Y_{i|i} \\ \hline Y_{i+1|2i-1} \end{array}\right] = \left[\begin{array}{c} Y_p^+ \\ \hline Y_f^- \end{array}\right]. \tag{2.90}$$

Therefore, considering the LQ decomposition in Eq. (2.85), the projection matrix and the output matrix $Y_{i|i}$ can be obtained as follows:

$$\Pi_{i-1} = Y_f^- / \underline{Y_p^+} = \begin{bmatrix} L_{31} & L_{32} \end{bmatrix} \begin{bmatrix} Q_1^T \\ Q_2^T \end{bmatrix} \tag{2.91}$$

$$Y_{i|i} = \begin{bmatrix} L_{21} & L_{22} \end{bmatrix} \begin{bmatrix} Q_1^T \\ Q_2^T \end{bmatrix} \tag{2.92}$$

Reversed controllability matrix Γ_i can be obtained from Eq. (2.63) as follows

$$\Gamma_i = O_i^\dagger T_{1|i}, \tag{2.93}$$

from which G matrix can be obtained extracting the last l columns. The initial output covariance R_0 can be obtained as

$$R_0 = \frac{1}{j} Y_{i|i} Y_{i|i}^T, \tag{2.94}$$

According to [13], three methods are available to estimate the state matrices A and C. The first method solves a least-squares problem on an overdetermined set of equations built from the Kalman state sequence $\hat{S}i = [\hat{s}_i, \hat{s}_{i+1}, ..., \hat{s}_{i+j-1}]$ from time i to $i+j-1$ [13], where ρ_w and ρ_v are residuals uncorrelated with the regressor $\hat{S}_i$.

$$\begin{bmatrix} \hat{S}_{i+1} \\ Y_{i|i} \end{bmatrix} = \begin{bmatrix} A \\ C \end{bmatrix} \hat{S}_i + \begin{bmatrix} \rho_w \\ \rho_v \end{bmatrix}, \tag{2.95}$$

$$\begin{bmatrix} A \\ C \end{bmatrix} = \begin{bmatrix} \hat{S}_{i+1} \\ Y_{i|i} \end{bmatrix} \hat{S}_i^{\dagger}. \tag{2.96}$$

All terms in Eq. (2.96) are numerically obtained by LQ decomposition.

The second method to estimate state matrices leverages the shifting nature of the observability matrix, identical to the SSI-cov method described in Eqs. (2.71)-(2.72).

$$O_i = \begin{bmatrix} C \\ CA \\ \vdots \\ CA^{i-1} \end{bmatrix} = \begin{bmatrix} O_i^{\uparrow} \\ CA^{i-1} \end{bmatrix} = \begin{bmatrix} C \\ O_i^{\downarrow} \end{bmatrix} \Rightarrow O_i^{\uparrow} = \begin{bmatrix} C \\ CA \\ \vdots \\ CA^{i-2} \end{bmatrix}, O_i^{\downarrow} = \begin{bmatrix} CA \\ CA^2 \\ \vdots \\ CA^{i-1} \end{bmatrix}$$

$$\Rightarrow \quad O_i^{\uparrow} A = O_i^{\downarrow} \quad \Rightarrow \quad A = {O_i^{\uparrow}}^{\dagger} O_i^{\downarrow}$$

Alternatively, it is possible to decompose with SVD the linear combination of $O_i^{\uparrow}$ and $O_i^{\downarrow}$ matrices, i.e.

$$\left[O_i^{\downarrow} - O_i^{\uparrow}\right] = U \Sigma V^T \quad \Rightarrow \quad V = \begin{bmatrix} V_{11} & V_{12} \\ V_{21} & V_{22} \end{bmatrix}, \tag{2.97}$$

$$A = V_{22} V_{12}^{-1} \tag{2.98}$$

with $V_{11}, V_{12}, V_{21}, V_{22} \in \mathbb{R}^{n \times n}$.

It is worth recalling that the first two methods do not mathematically guarantee positive realness of the state-sequence estimates; consequently, this also holds for the SSI-cov algorithm, which is based on the second approach (Eqs. (2.71)-(2.72)) [13, 19]. Indeed, the noise covariance estimates, and the matrices G and R_0, are unbiased under the assumption of infinitely long data. However, with finite-duration vibration-response records, these estimates may yield a state-space model whose states are neither real nor positive. In the frequency domain, this manifests as a synthesized spectrum that is not positive for every frequency line, which is mathematically meaningless. Theoretically, a forward innovation model cannot be obtained in such cases [13, 19], although in OMA the priority is typically robust modal-parameter estimation rather than an exquisitely accurate state-space model [13]. Nevertheless, when positive realness is a strict requirement, the third method for estimating the state matrices should be adopted. This approach uses the same least-squares setup as in the first method, i.e. Eq. (2.95), but leverages the residuals to estimate the nonsteady state covariance matrices of the noise

process (the innovation) in the Kalman-filter state-space formulation, so that

$$\frac{1}{j}\begin{bmatrix}\rho_w\\ \rho_v\end{bmatrix}\begin{bmatrix}\rho_w^T & \rho_v^T\end{bmatrix} = \begin{bmatrix}Q_i^{ww} & S_i^{wv}\\ [S_i^{wv}]^T & R_i^{vv}\end{bmatrix}\hat{S}_i^{\dagger}. \tag{2.99}$$

Since the Kalman filter converges unbiased with infinite data, the approximation for finite data introduces a bias but still ensures the positive realness of the states because the noise process covariance matrix in Eq. (2.99) is a positive-definite matrix for construction (all its eigenvalues are positive), i.e.

$$Q^{ww} = Q_i^{ww} \quad , \quad S^{wv} = S_i^{wv} \quad , \quad R^{vv} = R_i^{vv}. \tag{2.100}$$

The steady-state approximation ensures the validity of Eqs. (2.55)-(2.59), thus permitting to directly numerically solving the Riccati in order to obtain the forward innovation model [13].

Once the state matrices A and C are available, the modal parameters are obtained as in the SSI-cov method via Eq. (2.75), i.e., by solving the EVD of the state transition matrix A to find the Z-domain eigenvalues; mapping these back to the continuous Laplace domain yields natural frequencies, damped natural frequencies, and damping ratios. Also in SSI-dat, although the true model order n could, in principle, be inferred from the rank of the projection matrix, in practice it is unknown due to noise and often obscured by the absence of large SV gaps. Hence, a conservative stabilization-diagram approach is likewise employed here to identify stable pole alignments corresponding to the structure's physical modes. The stability checks are the same as in HVC Eqs. (2.77)–(2.78) and SVC Eqs. (2.79)–(2.81). Several SSI-dat variants appear in the literature, introducing weighting matrices $W_1 \in \mathbb{R}^{li\times li}$ and $W_2 \in \mathbb{R}^{j\times j}$ pre- and post-multiplying the projection matrix, i.e., $W_1\Pi_i W_2$, before the LQ decomposition [13]. The unweighted principal components (UPC) variant corresponds to the discussion so far, taking both W_1 and W_2 as identity; UPC SSI-dat is typically used when modes are well and uniformly excited and the SNR is good [13]. Conversely, the canonical variate analysis (CVA) SSI-dat is preferred for non-uniformly excited modes and noisier responses [13]. It employs the following weighting matrices:

$$W_1 = \left(\frac{1}{j}Y_pY_p^T\right)^{-1/2} \quad , \quad W_2 = I_{j\times j}. \tag{2.101}$$

Similarly to CVA SSI-cov, the SV of the weighted projection matrix can be interpreted as principal cosine angles between past output matrix row subspace and future output matrix row subspace [13]. Eventually, the principal component (PC) SSI-dat shows a compromise between CVA SSI-dat and UPC SSI-dat, so using the following weighting matrices:

$$W_1 = I_{li\times li} \quad , \quad W_2 = Y_p^T\left(\frac{1}{j}Y_pY_p^T\right)^{-1/2}Y_p. \tag{2.102}$$

Despite UPC, PC, and CVA having slightly different physical meanings, no significant differences in modal parameter estimate accuracy have been evidenced in the literature [13].

2.3 PyOMA and PyOMA2 for operational modal analysis

Within the field of SHM, operational modal analysis (OMA) is a well-established method for determining the dynamic properties of civil structures from the records of the ambient or output-only vibration. For many years, the majority of OMA implementations have been available only as MATLAB toolboxes, which can limit accessibility and integration with modern, open-source data science workflows. To overcome these limitations, a multi-institutional research effort involving the University of L'Aquila (Italy), the Norsk Treteknisk Institute in Oslo (Norway), and Politecnico di Torino (Italy) has led to the development of PyOMA, an open-source Python package dedicated to OMA [33].

The overall structure and goals of the PyOMA research project are summarized in Fig. 2.4. The project was conceived to provide a flexible and transparent environment for modal identification, fully based on the standard scientific Python ecosystem (NumPy, SciPy, Matplotlib, etc.), and to bridge the gap between advanced research algorithms and everyday engineering practice. The project focused especially on driving results reproducible, sharing open-source code, and ensuring that OMA tools could easily integrate into larger Python workflows for structural health monitoring, model updates, and data analysis.

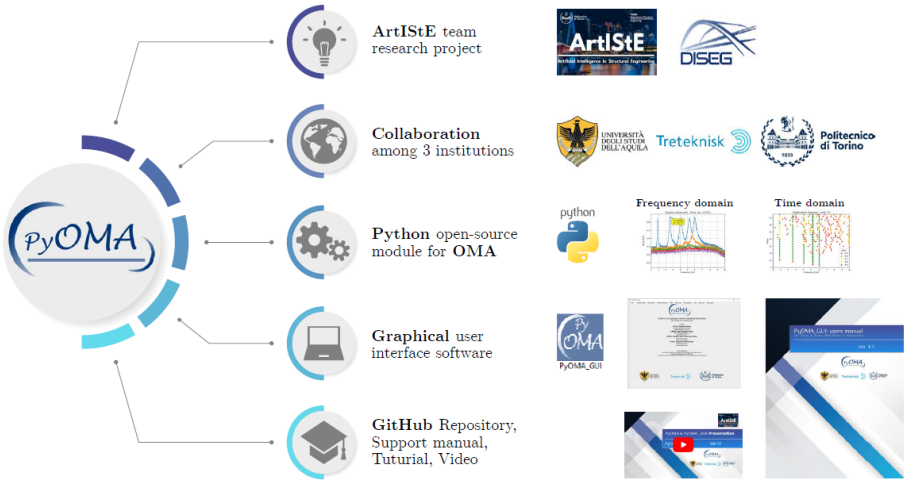

Figure 2.4: Schematic overview of the PyOMA research project and its main components.

2.3.1 Implemented algorithms in PyOMA

In its released version 1.5, the PyOMA package implements six widely used OMA algorithms, covering both frequency- and time-domain approaches [33]:

1. frequency domain decomposition (FDD) [34];
2. enhanced frequency domain decomposition (EFDD) [35];
3. frequency–spatial domain decomposition (FSDD) [36];
4. covariance-driven stochastic subspace identification (Cov-SSI) [37, 13];
5. data-driven stochastic subspace identification (DD-SSI) [19];
6. natural excitation technique – eigensystem realization algorithm (NExT–ERA) [13, 22].

These methods provide complementary views on the same underlying stochastic state-space model of the structure. Frequency-domain techniques (FDD, EFDD, FSDD) are particularly useful for obtaining initial estimates of natural frequencies and mode shapes, while time-domain methods (Cov-SSI, DD-SSI, NExT–ERA) enable more rigorous estimation of damping ratios and provide tools such as stabilization diagrams and clustering criteria. An overview of the algorithms implemented in PyOMA is shown in Fig. 2.5.

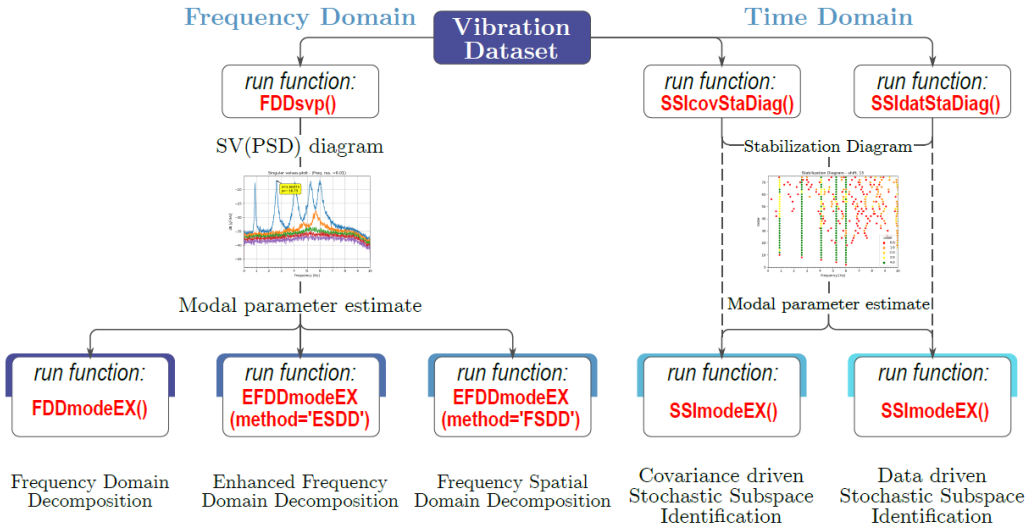

Figure 2.5: Overview of the OMA algorithms implemented in the PyOMA toolbox.

In the context of the present thesis, this set of algorithms is particularly relevant because it includes both the frequency-domain FDD method and the covariance-driven SSI formulation, which constitute the core of the identification pipeline adopted to track damage evolution in the tested reinforced-concrete buildings.

2.3.2 Graphical user interface PyOMA_GUI

While PyOMA can be used directly as a Python module, the project also provides a dedicated graphical user interface, PyOMA_GUI, intended for users who prefer a more interactive workflow or who are less familiar with Python scripting. PyOMA_GUI is distributed as an open-source application and is built on top of the same underlying Python routines that form the PyOMA package.

From a user perspective, PyOMA_GUI guides the analyst through the complete OMA workflow, including:

- import of measurement data from different file formats;
- definition of the structural geometry and assignment of measurement channels and degrees of freedom (DOFs);
- basic preprocessing of the acquired time histories (detrending, resampling, decimation, filtering);
- execution of the dynamic identification algorithms (FDD, EFDD, FSDD, Cov-SSI, DD-SSI, NExT–ERA) with interactive visualization of spectra, singular value plots, stabilization diagrams, and mode shapes;
- post-processing and export of the identified modal parameters for further analyses, including model updating or long-term SHM.

A schematic representation of the main components and data flow within PyOMA_GUI is reported in Fig. 2.6. Although the present thesis relies primarily on Python scripts and Jupyter notebooks for batch processing of the large test dataset, the design philosophy of PyOMA_GUI is consistent with the needs of this work: enabling reproducible analyses while also supporting quick visual inspection and quality control of the identified modes.

2.3.3 From PyOMA to PyOMA2

More recently, the original PyOMA implementation has evolved into a second-generation toolbox, *PyOMA2*[1], which reorganizes and significantly extends the capabilities of the package [11]. The new logo of PyOMA2 is shown in Fig. 2.7, emphasizing the continuity with the original project while highlighting the modular and extensible architecture of the new code.

PyOMA2 is structured into three main layers:

- **Data and experiment layer:** this level provides classes to store and manage measurement data, metadata, sensor layouts, test configurations, and processing

[1] `https://github.com/dagghe/PyOMA2`

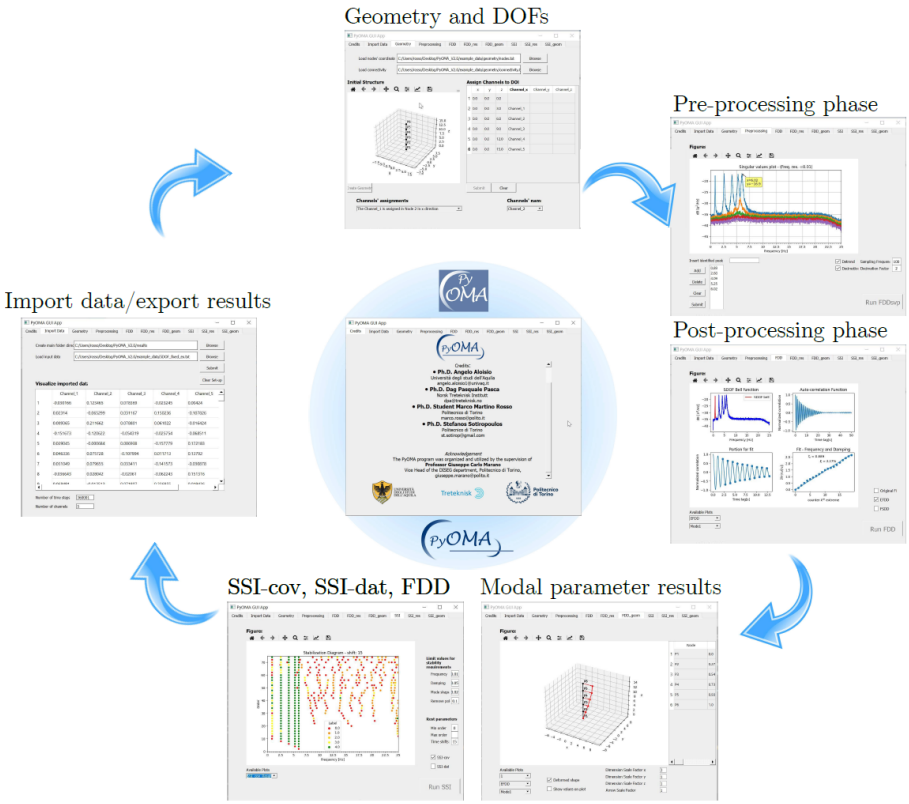

Figure 2.6: General overview of the PyOMA_GUI graphical user interface and its main workflow steps.

Figure 2.7: Logo of the PyOMA2 toolbox, the second-generation implementation of PyOMA.

parameters. It supports both single-setup and multi-setup experiments, including tests with reference and roving sensors, which are common in civil engineering applications [27].

- **Algorithm layer:** this level contains the implementations of the identification algorithms. Each algorithm is encapsulated in a dedicated class, which receives data objects as input and returns modal estimates, together with diagnostic plots such as singular value spectra, stabilization diagrams, and mode-shape animations.

- **Visualization and utilities layer:** this level includes functions for animating mode shapes, interacting with the generated plots, and performing auxiliary tasks (e.g., selection of stable poles, computation of MAC values, or export of identified

modes to external formats).

In addition to reorganizing the code structure, PyOMA2 extends the range of supported methods. Besides the frequency-domain approaches (FDD, EFDD, FSDD) and the time-domain Cov-SSI and DD-SSI algorithms already present in PyOMA, PyOMA2 introduces the Polyreference Least Squares Complex Frequency (pLSCF) / Polymax method [13]. This offers further flexibility for frequency-domain modal identification, especially in cases where closely spaced modes or higher damping require more sophisticated curve-fitting strategies.

2.3.4 Role of PyOMA2 in the present thesis

In this thesis, PyOMA2 is used as the main Python toolbox for processing the acceleration time histories recorded on the two full-scale, three-dimensional reinforced-concrete test buildings subjected to shaking table tests). The workflow implemented in PyOMA2 for this work can be summarized as follows:

1. import of the raw acceleration records from the dense sensor network installed on both the as-built and retrofitted frames;

2. preprocessing steps consistent with the general data treatment adopted in this thesis (orientation of sensor axes, time alignment across tests, interpolation, anti-alias filtering, and optional decimation to the analysis sampling rate);

3. application of FDD to obtain initial estimates of natural frequencies and preliminary mode shapes at each damage state for both structures;

4. application of covariance-driven SSI to refine the modal estimates, construct stabilization diagrams, and extract stable poles across model orders, exploiting the tools available in PyOMA2 for clustering and MAC-based mode selection;

5. export of the identified modal parameters and mode shapes for comparison with the finite-element baseline model developed in the Scientific Toolkit for OpenSees (STKO) and for tracking the evolution of modal properties with increasing seismic excitation.

Although PyOMA2 also provides implementations of DD-SSI and additional identification techniques, the main results reported in this thesis are based on the combination of FDD and Cov-SSI, which has proven robust and computationally efficient for the large dataset considered. The use of an open-source, Python-based toolbox ensures that the complete identification process is fully reproducible, facilitating future extensions, such as automated monitoring, real-time damage tracking, or integration with machine learning models for structural health monitoring.

2.4 MATLAB OoMA toolbox

In addition to the Python-based workflows, a number of open toolboxes for operational modal analysis (OMA) have been developed in the MATLAB environment over the last decade. Among these, the *OoMA* (Output-Only / Operational Modal Analysis) toolbox by Otto has become a widely used, freely available resource for output-only modal identification in civil, mechanical, and aerospace applications [38]. The toolbox is distributed through the MATLAB Central File Exchange and provides a set of functions specifically tailored to stochastic subspace identification (SSI) and frequency-domain decomposition (FDD) of OMA, which can be easily integrated into existing MATLAB workflows. The OoMA toolbox was conceived to offer a compact, script-oriented implementation of output-only modal analysis algorithms that exposes intermediate quantities such as block Hankel matrices, stabilization diagrams, and MAC values. In contrast to large commercial packages, the code emphasizes transparency of the identification procedure and the possibility of modifying or extending the routines for research purposes. The theoretical background for the implemented methods follows standard references on operational modal analysis and subspace-based system identification [13].

2.4.1 Implemented algorithms and core functions

The core of the OoMA toolbox consists of several identification routines centered on stochastic subspace identification, complemented by a frequency-domain method for initial estimation of modal properties [38]. The main algorithms documented in the toolbox are:

- covariance-driven stochastic subspace identification (SSI-COV), based on auto- and cross-covariance sequences of the outputs;
- data-driven stochastic subspace identification (SSI-DATA), operating directly on Hankel matrices built from the measured time histories;
- covariance-driven SSI with reference channels (SSI-COV/REF), for multi-setup or multi-reference experiments;
- a frequency-domain identification function compatible with the Frequency Domain Decomposition (FDD) method, which can also be used together with the dedicated FDD implementation by Farshchin [39].

Alongside these high-level routines, OoMA provides helper functions to support the complete OMA workflow, such as:

- construction of block Hankel matrices from multi-channel time series;
- generation and interactive inspection of stabilization diagrams;
- computation of the Modal Assurance Criterion (MAC) and MAC matrices;

- organization and export of identified modal parameters (frequencies, damping ratios, and mode shapes).

These tools allow the user to move from raw accelerations to stabilized modal estimates and provide diagnostics for assessing the quality and physical meaning of the identified modes.

The toolbox is distributed as a standard MATLAB toolbox file and a compressed archive that can be downloaded from the File Exchange page [38], where example Live Scripts are also provided to illustrate typical use cases. The distribution includes a recommended "Cite As" entry so that users can properly acknowledge the toolbox in scientific publications.

2.4.2 Use in recent research and applications

Since its release, the MATLAB OoMA toolbox has been adopted in several peer-reviewed studies as the main implementation of SSI-based OMA or as a reference method. Use SSI-COV as implemented in OoMA to track accelerated corrosion damage in a steel beam via an ARMA-based damage index [40]. Hakim et al. employ functions from the OoMA toolbox to construct stabilization diagrams and extract natural frequencies when studying the effect of corrosion damage on the dynamic properties of reinforced-concrete buildings [41]. Cardoni et al. refer to OoMA as one of the OMA tools used when proposing a refined output-only modal identification technique for structural health monitoring of civil infrastructures [42]. These examples illustrate that OoMA is not only a teaching or demonstration toolbox, but a practical tool used in real test campaigns and structural health monitoring research.

2.4.3 Role of OoMA in the present thesis

In the present thesis, the MATLAB OoMA toolbox is used in parallel with the Python-based PyOMA2 framework (Section 2.3) to perform cross-validation of the identified modal parameters. Specifically, the acceleration records from the shaking table tests on the two full-scale reinforced-concrete buildings are processed in OoMA using:

1. covariance-driven SSI (SSI-COV) to construct stabilization diagrams and extract stable poles across model orders;

2. data-driven SSI (SSI-DATA) and, where necessary, SSI-COV with reference channels (SSI-COV/REF) to verify the robustness of the identification under alternative formulations and multi-setup configurations;

3. a frequency-domain FDD-type analysis as an additional check on the natural frequencies and qualitative mode shapes obtained for selected damage states, optionally compared to the dedicated FDD toolbox [39].

The modal estimates obtained with OoMA are compared to those produced by PyOMA2 and to the finite-element baseline model developed in the Scientific Toolkit for OpenSees (STKO). Consistency between the MATLAB- and Python-based workflows in terms of natural frequencies, damping ratios, and MAC values for the principal modes provides an important validation of the overall identification chain and increases confidence in the trends used to monitor damage evolution and retrofit effectiveness.

Chapter 3

Case study: full-scale RC buildings on a shaking table

3.1 Overview of the experimental campaign

The case study considered in this thesis consists of two nominally identical, full-scale, three-dimensional reinforced-concrete (RC) frame buildings tested on a unidirectional shaking table at the University "G. d'Annunzio" of Chieti–Pescara. The buildings are mounted side by side on a common RC foundation slab rigidly fixed to the shaking table. The superstructures are not connected to each other and can therefore be studied as two independent specimens subjected to the same base excitation.

One of the buildings is in an as-built configuration (Building 1), whereas the second building (Building 2) is equipped with a proprietary seismic retrofitting system that mainly targets an increase in lateral stiffness and a modification of the global dynamic response. The retrofit details are covered by an ongoing patent process and cannot be disclosed in this thesis, but the two specimens are otherwise identical in terms of geometry, mass distribution, and material properties. A schematic view of the geometry and reinforcement layout of the columns, slabs, and foundation is shown in Fig. 3.1. A photograph of the two buildings installed on the shaking table is reported in Fig. 3.2.

3.2 Geometry, materials, and structural configuration

Each frame has a rectangular plan of $5.00\,\mathrm{m} \times 2.00\,\mathrm{m}$. The three floor levels are located at heights of 2.90 m, 5.80 m, and 8.84 m above the base plate, with a clear inter-storey height of approximately 2.50 m. The vertical load-resisting system consists of RC columns with square cross-section of $0.20\,\mathrm{m} \times 0.20\,\mathrm{m}$, reinforced with four φ16 mm longitudinal bars (longitudinal reinforcement ratio of about 2%) and closed φ8 mm stirrups. Transverse reinforcement is spaced at 100 mm along the column height, with closer spacing (50 mm) in the plastic hinge regions near the base to improve ductility.

The floor system is a solid RC slab with a total thickness of approximately 0.40 m

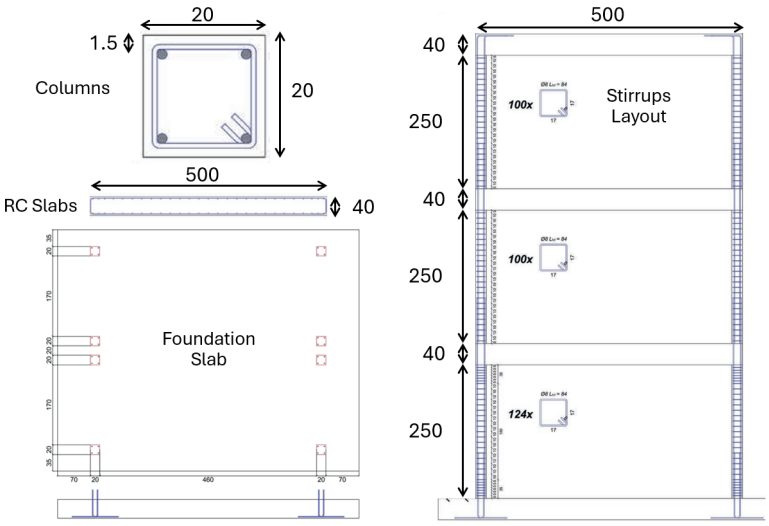

Figure 3.1: Geometric and reinforcement details of the RC columns, slabs and foundation slab (dimensions in cm).

Figure 3.2: Twin full-scale RC buildings mounted on the unidirectional shaking table. Building 1 (left) is as-built; Building 2 (right) is retrofitted.

and symmetric smeared bending reinforcement using φ16 mm bars. The perimeter brick infills and internal partitions are installed on the upper storeys to reproduce realistic mass and stiffness contributions of typical building envelopes. Both frames are cast with concrete class C30/37 and B450C reinforcing steel, consistent with common European design practice.

The same buildings had already been used in previous shaking table tests investigating a servo-hydraulic active mass damper (AMD) system, as documented in [8]. To guarantee comparable mass conditions between the current and previous test configurations, the weight of the removed device was compensated by increasing the thickness of the top slab of both specimens. As a result, the two buildings share the same geometry, material properties, and mass distribution, with the only substantial difference being the presence of the retrofit system in one of them.

In addition to the RC structural system, the laboratory setup includes an internal steel safety frame located in the central bay between the two buildings. The frame is composed of a vertical steel column, and it is bolted to the foundation slab at the bottom and to the slab of the third floor at the top, as shown in Fig. 3.3. Its primary function is to prevent catastrophic collapse of the specimens in case of severe damage during the high-intensity shaking-table tests, ensuring the safety of the laboratory and the equipment. Under the moderate vibration levels used for the white-noise tests and the lower-intensity Irpinia runs, the safety frame is not expected to carry significant load; however, some interaction with the RC frames can occur at larger lateral displacements, and its possible influence on the identified dynamic properties will be discussed in the next chapters.

Figure 3.3: View of the two RC buildings on the shaking table with the internal steel safety frame in the central bay. The frame is bolted to the foundation slab and to the slab of the third floor and is used as a safety device during the shaking-table tests.

3.3 Instrumentation and sensor layout

The structures are instrumented with 40 low-power triaxial sensors connected to Ethernet switches. Each sensing unit is based on the ASDEA MonStr device, a MEMS-technology unit equipped with a triaxial accelerometer, gyroscope, inclinometer, magnetometer and thermometer. The power consumption of each device is extremely low (about 0.6 W), and the units are certified IP68 with full water and dust protection, able to operate nominally in the temperature range from $-20°C$ to $+70°C$.

Of the 40 sensors, two were mounted to measure the input motion from the shaking table: one attached directly to the table and one attached to the RC foundation slab. The remaining 38 sensors were distributed evenly between the two specimens, with 19 units on each building, installed on the RC frames as well as on the internal partitions and infill walls.

For the purposes of the OMA performed in this thesis, only the accelerometers installed at (or very close to) the RC frame nodes and aligned with the global shaking direction are used. This choice focuses the analysis on the primary lateral degrees of freedom and avoids the influence of possible local panel modes in the infills. The selected channels correspond to three storey levels per building, with one sensor at the top of each column line, giving six effective sensors per building. It is worth noting that, due to installation constraints, the sensor at the third floor in each building is not located exactly at the ideal beam–column node but is positioned a short distance away along the slab edge. Given the small offset relative to the bay dimensions, the sensor is nevertheless associated with the corresponding frame node in the modal analysis, and its influence on the identified global modes is considered negligible.

The adopted OMA sensor layout is depicted in Fig. 3.4, where Building 1 (as-built) and Building 2 (retrofitted) are shown separately together with the sensor identifiers used in the dataset.

The coordinates of the twelve sensors used for OMA are reported in Table 3.1. They are expressed in the global reference system adopted for the experimental setup, with X along the shaking-table direction, Y in the transverse horizontal direction and Z vertical.

All sensors record accelerations with a nominal sampling rate of 1 kHz. The acquisition architecture is asynchronous: each unit relies on its own local clock and time-stamps the measurements using an absolute time reference. This is a typical strategy in wireless or distributed structural health monitoring systems and requires dedicated post-processing to reconstruct a common uniform time axis for all channels [10].

3.4 Shaking table input protocol

The buildings were tested on a unidirectional shaking table, excited along the global X direction. The input history was designed to reproduce an earthquake–sequence

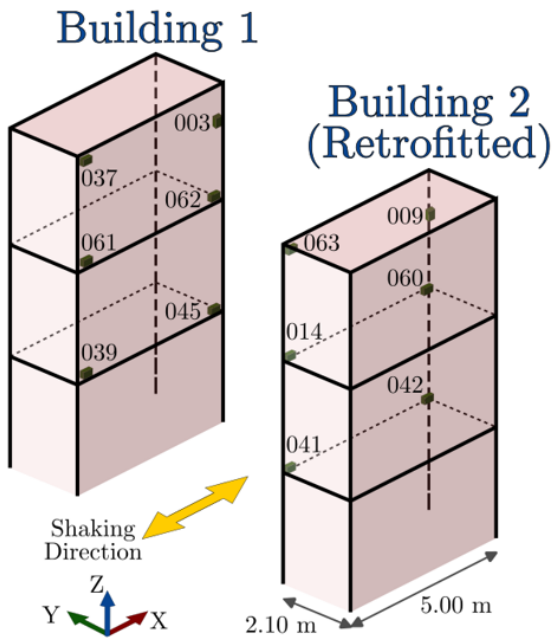

Figure 3.4: Sensor layout used for OMA in the case study. Only the accelerometers located at (or very close to) the RC frame nodes in the direction of shaking are considered in this thesis.

Table 3.1: Coordinates of the accelerometers used for OMA (global reference system, units in mm).

Sensor	**X [mm]**	**Y [mm]**	**Z [mm]**
MNAT0003	67698	2362	7825
MNAT0037	62698	2362	8840
MNAT0039	62698	2362	2900
MNAT0045	67698	2362	2900
MNAT0061	62698	2362	5800
MNAT0062	67698	2362	5800
MNAT0009	67698	2362	7825
MNAT0014	62698	2362	5800
MNAT0041	62698	2362	2900
MNAT0042	67698	2362	2900
MNAT0060	67698	2362	5800
MNAT0063	62698	2362	8840

-type loading, in which the structures experience a series of increasing seismic demands interspersed with low-amplitude white-noise excitations suitable for operational modal analysis.

The seismic component of the protocol is based on a real accelerogram recorded during the 1980 Irpinia earthquake in southern Italy [9]. Let $a_{\mathrm{Irp}}(t)$ denote this reference acceleration time history. In the tests, scaled versions of $a_{\mathrm{Irp}}(t)$ were applied to the

shaking table so as to reach different peak ground acceleration (PGA) levels. The sequence of Irpinia runs is as follows:

- **Irpinia Ladder 25%** (Day 1): three consecutive applications of the Irpinia record, scaled such that the corresponding PGAs are 0.046 g, 0.083 g, and 0.086 g. The three runs have an individual duration of 24 s, leading to a total ladder duration of 72 s (24×3);
- **Irpinia 50%** (Day 1): single application of the scaled Irpinia record with PGA 0.202 g and duration 24 s;
- **Irpinia 75%** (Day 2): single application with PGA 0.376 g and duration 24 s;
- **Irpinia 100%** (Day 2): single application with PGA 0.440 g and duration 24 s;
- **Irpinia 125%** (Day 2): single application with PGA 0.616 g and duration 24 s.

Between the Irpinia runs, the buildings were excited with stationary Gaussian white noise. These white-noise tests were designed to satisfy the typical assumptions of operational modal analysis broadband input, approximately flat power spectral density in the frequency band of interest, and relatively low amplitude so as to remain in the weakly nonlinear or quasi-linear regime. The white-noise motions have standard deviations of approximately 0.01 g and a nearly constant power spectral density of about -60 dB in the 0–50 Hz frequency range. For each test, the table controller also reports an equivalent PGA, which is used here as a compact measure of input intensity.

Table 3.2 summarises the full shaking-table protocol over the two test days, including PGAs, standard deviations and durations for both the Irpinia and white-noise inputs. The white-noise tests numbered 2 and 3 provide the reference "initial-condition" modal properties, while the subsequent white-noise records (4 to 7) are used to monitor the evolution of modal parameters as damage accumulates due to the progressively more severe Irpinia excitations.

3.5 Data acquisition and preprocessing

All acceleration time histories are recorded in an HDF5 database and exported for offline processing. Due to the asynchronous acquisition scheme, the start times and sampling instants of the different channels do not perfectly coincide, and small clock drifts occur over the duration of the tests. In addition, the orientation of the sensor axes differs from unit to unit, depending on how the devices are mounted on the structural elements.

To obtain a consistent dataset for OMA, the following preprocessing steps are carried out:

Table 3.2: Excitation input protocol: sequence of scaled Irpinia waveform and white noise shaking inputs.

Day of Test	Shaking table test sequences	PGA [g]	Dev. Std. [g]	Duration [s]
27/06/2022	Irpinia Ladder 25%	(0.046; 0.083; 0.086)	–	$24 \cdot 3 = 72$
	White Noise 2	0.070	0.011	160
	White Noise 3	0.064	0.011	320
	Irpinia 50%	0.202	–	24
	White Noise 4	0.067	0.009	160
28/06/2022	Irpinia 75%	0.376	–	24
	White Noise 5	0.076	0.011	160
	Irpinia 100%	0.440	–	24
	White Noise 6	0.068	0.012	160
	Irpinia 125%	0.616	–	24
	White Noise 7	0.079	0.011	160

1. **Coordinate transformation:** each triaxial accelerometer record is rotated from the local sensor axes to the global structural axes using the known installation orientations, so that all channels are expressed in a common (X, Y, Z) reference system;

2. **Time synchronisation:** using the absolute time-stamps and following the strategy proposed for asynchronous sensor networks in [10], all channels are numerically interpolated onto a common uniformly spaced time grid with effective sampling frequency 1 kHz, aligning the data to the fastest clock;

3. **Filtering and decimation:** to reduce high-frequency noise and avoid aliasing, the signals are first mapped to a finer grid, low-pass filtered using an anti-alias finite impulse response (FIR) filter, and then decimated to the analysis sampling rate adopted in the subsequent OMA (200 Hz);

4. **Selection of stationary windows and channels:** for each white-noise test, the stationary portion of the records is extracted and the subset of channels corresponding to the frame sensors shown in Fig. 3.4 is retained for modal identification.

The resulting synchronised and filtered acceleration time histories form the basis for the frequency-domain and time-domain identification procedures described in section 2.2. In particular, the data are analyzed using the PyOMA2 toolbox (Section 2.3) and the MATLAB OoMA toolbox (Section 2.4) in order to estimate and track the evolution of modal parameters for both the as-built and the retrofitted buildings under increasing levels of seismic demand.

Chapter 4

Experimental data processing and OMA pipeline

This chapter presents the operational modal analysis (OMA) procedure adopted in this thesis to identify the dynamic properties of the two full-scale RC buildings described in Chapter 3. The aim is to obtain robust estimates of natural frequencies, damping ratios and mode shapes at different damage states, starting from raw acceleration measurements recorded during white-noise excitations.

The workflow consists of: (i) pre-processing of the acceleration signals (import, time alignment, resampling, orientation, trimming, detrending and decimation); (ii) frequency-domain identification based on Frequency Domain Decomposition (FDD, specifically an EFDD/FSDD-type approach); and ((iii) time-domain identification using covariance-driven stochastic subspace identification (SSI-COV). The same methodology and parameter choices are applied consistently in both software environments used in this work.

4.1 Data import, time alignment and resampling

Acceleration records are acquired by the MonStr sensor network (Section 3.3) and stored in HDF5 files, one per test. For each white-noise test and each building, the following quantities are imported for all relevant sensors:

- the three components of acceleration in the sensor-local reference system, expressed in raw counts;
- the associated time stamps, expressed in absolute time.

The raw counts are converted into physical units through a constant gain factor, such that the accelerations are expressed directly in units of gravitational acceleration g. For each device this yields three time series $a_x(t_i)$, $a_y(t_i)$, $a_z(t_i)$ defined on a (slightly irregular) time grid t_i.

Since all MonStr units rely on independent clocks, the start times and sampling instants of different devices do not coincide exactly. To obtain a common time origin, the absolute time-stamp of the first sample is extracted for each sensor and the minimum of these values is subtracted from all time vectors. In this way, all channels share a consistent reference time, although small differences in sampling intervals remain.

To perform modal analysis it is convenient to work with a regular grid. A target sampling frequency of $f_{\text{target}} = 2000$ Hz is selected and a common time vector

$$t^* = \{0, \Delta t, 2\Delta t, \ldots, T_{\min}\}, \qquad \Delta t = 1/f_{\text{target}},$$

is created, where $T_{\min}$ is the minimum record length across all channels. For each sensor and each component, the original time series is interpolated onto this grid using linear interpolation,

$$\tilde{a}_k(t^*) = \text{interp}\big(t^*,\, t_i,\, a_k(t_i)\big), \qquad k \in \{x, y, z\}, \tag{4.1}$$

so that all channels are uniformly sampled on the same time vector.

The interpolation step has two main purposes: (i) to remove the small clock jitters inherent to the asynchronous acquisition of the MonStr units, and (ii) to obtain a single, uniformly sampled multi-channel record suitable for frequency-domain and time-domain identification. Let $t_i^{(s)}$ denote the shifted time stamps of sensor s (after subtracting the minimum initial time across all channels) and $a_k^{(s)}(t_i^{(s)})$ the corresponding samples for component $k \in \{x, y, z\}$. Because each device runs on its own clock, the grids $\{t_i^{(s)}\}$ are only approximately uniform and differ slightly from sensor to sensor, even though their mean sampling frequency is close to the nominal value.

A common regular grid t^* is therefore introduced as above, with $f_{\text{target}} = 2000$ Hz and $T_{\min}$ equal to the shortest record length among all channels. For each sensor and each component, the original samples are projected onto this grid by linear interpolation,

$$\tilde{a}_k^{(s)}(t_j^*) = \text{interp}\big(t_j^*;\, t_i^{(s)}, a_k^{(s)}(t_i^{(s)})\big), \qquad j = 0, \ldots, N^* - 1,$$

so that all channels become uniformly sampled on the same time vector t^*.

This interpolation-based synchronization follows typical strategies developed for asynchronous structural-health-monitoring sensor networks, where absolute time stamps are used to reconstruct the individual sampling instants and then all records are resampled onto a common, finer grid before modal analysis [10, 1]. Provided that the local clock jitter remains small with respect to Δt, the induced amplitude and phase errors are negligible in the frequency band of interest and do not bias the estimated modal parameters.

4.2 Channel selection and orientation into the global frame

The accelerometers are mounted on the RC frames, partitions and infill walls of both buildings, with each MonStr unit having its own local reference axes. The test documentation provides, for each device:

- whether it is located on the RC frame, on partitions/infill, or used as an input sensor (table and foundation slab);
- which local axes correspond to the global directions X, Y and Z, including the sign convention (e.g. +X, -Y, +Z).

For OMA, only the sensors on the RC frames are retained and only the components aligned with the global shaking plane are used. In particular:

- sensors on the RC frames are selected by means of a flag in the metadata; this yields 19 devices per building;
- sensors on partitions and infills are ignored for OMA, as they mainly capture local panel modes;
- for each frame sensor, two global directions are defined, associated with the global X (shaking direction) and Y axes, respectively.

The orientation of each sensor is modeled by a simple orthogonal transformation between the local and global axes. Since the devices are installed with their local axes approximately aligned with the building axes, this transformation reduces to selecting, for each sensor, the appropriate local component and applying the correct sign to obtain the global X and Y responses. The mapping between local and global directions (e.g. global X corresponding to local $-Y$ for a given device) can differ from sensor to sensor, and it is fully specified in the test documentation through axis labels and sign conventions. In this way, two horizontal acceleration components are associated with each frame sensor, representing the response along the global shaking direction and the transverse horizontal direction.

The third, nominally vertical, component is retained during the basic pre-processing but is not used in the subsequent modal identification. Since the shaking table applies purely horizontal excitation and the buildings are much more flexible in the lateral directions than in the vertical one, the vertical degrees of freedom are only weakly excited and weakly coupled with the horizontal modes. Their natural frequencies are expected to lie at much higher values (associated with local slab and floor vibrations), outside the frequency band of interest for the global lateral modes. Neglecting the vertical components therefore does not affect the identified lateral natural frequencies and mode shapes, while it simplifies the data set and improves the numerical conditioning of the OMA procedures.

Due to installation constraints, the sensor at the third floor of each building is not located exactly at the theoretical beam–column node but a short distance away along the slab. Given the relatively small offset compared to the bay dimensions, these devices are still associated with the corresponding frame nodes in the modal analysis.

The input sensors on the shaking table and foundation slab are processed in the same way, ensuring that positive acceleration corresponds to motion in the positive global X direction.

The effect of the orientation step is illustrated in Fig. 4.1, which compares the three acceleration components of one sensor in the original local axes and after rotation into the global frame. After rotation, the static gravity component is almost entirely aligned with the global vertical direction, while the horizontal components oscillate around zero, confirming the correctness of the adopted convention.

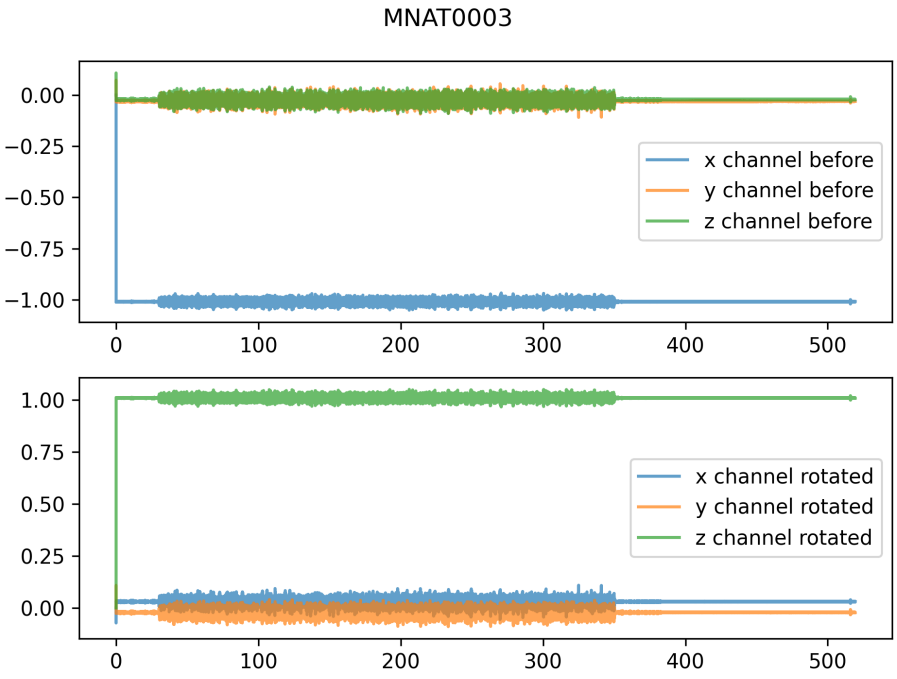

Figure 4.1: Example of orientation correction for sensor MNAT0003. Top: accelerations in the sensor-local axes. Bottom: accelerations after rotation into the global frame. The gravity component is concentrated in the global vertical direction, while the horizontal components oscillate around zero.

4.3 Selection of stationary windows, detrending and decimation

Although the white-noise tests are nominally stationary, the start and end of each record are affected by the ramp-up and ramp-down of the shaking-table controller. To ensure that only stationary segments are used, each resampled record is inspected

and an inner time window is selected. For White Noise 2, used as a reference case in this thesis, the interval $[t_{\text{start}}, t_{\text{end}}] = [12\text{ s}, 172\text{ s}]$ is chosen, leading to a duration of $T_{\text{OMA}} = 160$ s. Similar criteria are applied to the other white-noise tests.

The global acceleration components from all frame sensors are then assembled into a data matrix

$$\mathbf{Y}(t_n) = \left[a_{X,1}^{\text{glob}}(t_n) \quad a_{Y,1}^{\text{glob}}(t_n) \quad \dots \quad a_{X,N}^{\text{glob}}(t_n) \quad a_{Y,N}^{\text{glob}}(t_n) \right], \tag{4.2}$$

where $N = 6$ is the number of frame sensors per building and t_n are the discrete time instants within the selected window.

Before identification, each column of $\mathbf{Y}$ is detrended to remove any constant offset or linear drift. This is done by subtracting the least-squares linear fit of each time series, yielding a zero-mean, trend-free dataset.

To reduce computational cost and eliminate unnecessary high-frequency content, the detrended data are then decimated by an integer factor $q = 10$. The procedure consists of a low-pass anti-alias FIR filter followed by downsampling, leading to an effective sampling frequency

$$f_s = \frac{f_{\text{target}}}{q} = \frac{2000}{10} = 200 \text{ Hz}.$$

The associated Nyquist frequency of 100 Hz is largely sufficient, since all modes of interest lie below 25 Hz. The same decimation strategy and parameters are used in both software implementations.

To verify that the preprocessed white-noise records satisfy the standard assumptions of OMA (approximately stationary, zero-mean, nearly Gaussian response, broadband excitation), diagnostic "info plots" are inspected for representative channels before and after the preprocessing steps. Each info plot combines the time history, the normalised auto-correlation, the probability density function (PDF), the power spectral density (PSD) and a normal probability (Q–Q) plot, following common practice in OMA data screening [1].

Figure 4.2 shows an example for one response channel after time alignment and interpolation but before selection of the stationary window and decimation. The time history still contains initial and final transients, and the PSD extends beyond the frequency band of interest. The PDF is sharply peaked due to the presence of spikes, and slight deviations from a straight line are visible in the normal probability plot.

After extracting the stationary portion of the record, removing the mean, and applying the anti-alias filtering and decimation to the analysis sampling rate, the corresponding info plot in Fig. 4.3 exhibits a much more stationary signal. The PSD is approximately flat up to about 50 Hz and then decays rapidly, the auto-correlation function quickly converges to zero, and both the PDF and Q–Q plot indicate a response that is close to Gaussian. These checks support the validity of the OMA assumptions

for the processed records used in the subsequent FDD and SSI analyses.

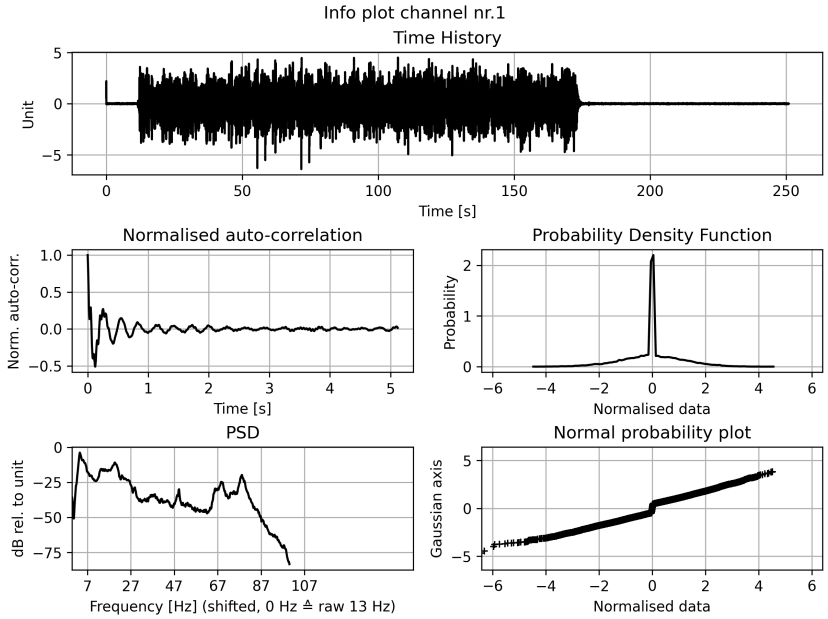

Figure 4.2: Example "info plot" before selection of the stationary window and decimation. The subplots show the time history, normalized auto-correlation, probability density function, power spectral density and normal probability plot.

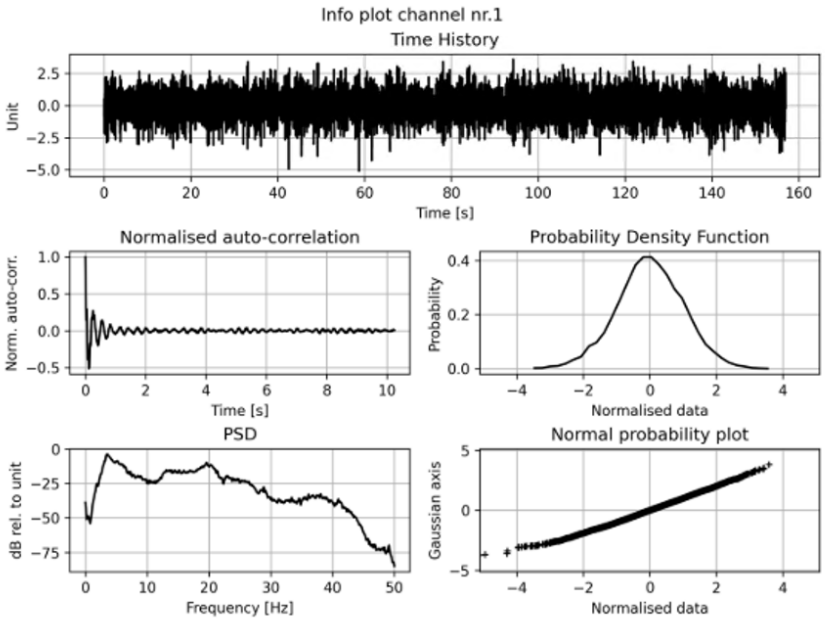

Figure 4.3: Info plot of the same channel after extraction of the stationary white-noise window, detrending and decimation to the analysis sampling rate. The response is approximately stationary, the PSD is nearly flat in the 0–50 Hz band, and the marginal distribution is close to Gaussian.

4.4 Frequency-domain identification: FDD / FSDD

The first step of modal identification is carried out in the frequency domain using Frequency Domain Decomposition (FDD) [34, 36]. The method operates on the cross-power spectral density (PSD) matrix $\mathbf{S}_{yy}(\omega)$ of the output vector $\mathbf{Y}(t)$, estimated via Welch's method from the decimated data. At each discrete circular frequency ω_k, a singular value decomposition is performed,

$$\mathbf{S}_{yy}(\omega_k) = \mathbf{U}(\omega_k)\,\mathbf{\Sigma}(\omega_k)\,\mathbf{U}^H(\omega_k), \tag{4.3}$$

where $\mathbf{\Sigma}(\omega_k)$ is a diagonal matrix containing the singular values $\sigma_1(\omega_k) \geq \sigma_2(\omega_k) \geq \ldots$ and $\mathbf{U}(\omega_k)$ contains the corresponding singular vectors.

The first singular value $\sigma_1(\omega)$ is commonly referred to as the complex mode indicator function (CMIF). Peaks of the CMIF indicate candidate natural frequencies, and the first singular vector at those frequencies provides estimates of the associated mode shapes. In this work an enhanced version of FDD, often termed EFDD or FSDD, is used: around each CMIF peak, a narrow frequency band is selected and an inverse Fourier transform of the corresponding single-degree-of-freedom spectral bell is computed to obtain an approximate impulse response function, from which damping ratios can also be estimated [36].

The CMIF plots obtained for each white-noise test are used primarily to identify the approximate positions of the main modes and to support the interpretation of the stabilization diagrams described in the next section.

4.5 Time-domain identification: covariance-driven SSI

The main modal identification is performed in the time domain using covariance-driven stochastic subspace identification (SSI-COV) [37, 13, 19]. The structural response is modeled as a discrete-time linear stochastic state-space system,

$$\mathbf{x}_{k+1} = \mathbf{A}\,\mathbf{x}_k + \mathbf{w}_k, \tag{4.4}$$

$$\mathbf{y}_k = \mathbf{C}\,\mathbf{x}_k + \mathbf{v}_k, \tag{4.5}$$

where $\mathbf{x}_k$ is the state vector, $\mathbf{y}_k$ is the output vector (accelerations), and $\mathbf{w}_k$, $\mathbf{v}_k$ are zero-mean white-noise processes. The matrices $\mathbf{A}$ and $\mathbf{C}$ contain the system dynamics and the modal information to be identified. In the covariance-driven formulation, the information required for identification is encoded in the output covariance matrices,

$$\mathbf{R}_{yy}(\ell) = \mathbb{E}\left[\mathbf{y}_k \mathbf{y}_{k+\ell}^T\right], \tag{4.6}$$

which are estimated empirically from the measured outputs for a range of time lags ℓ. These covariance matrices are arranged into a block Toeplitz matrix from which an

extended observability matrix is identified by means of singular value decomposition. The system matrix $\mathbf{A}$ is then obtained via least-squares regression, and its eigenvalues and eigenvectors are used to compute modal properties. The method is applied for a range of model orders up to a maximum order $n_{\max}$. In this thesis, the number of block rows is taken as $b_r = 80$, providing a sufficient delay range to capture the dynamics of interest, and the maximum model order is set to $n_{\max} = 2b_r = 160$. A stabilization diagram is then built by plotting the identified poles in the frequency–order plane and assessing their stability as the model order increases. A pole is considered *stable* when its natural frequency, damping ratio and mode shape change only slightly between successive orders and when the mode shapes have a high Modal Assurance Criterion (MAC) [12]. The stabilization diagram is examined in conjunction with the CMIF peaks from FDD to select stable poles associated with the physical modes. For each mode of interest, a representative model order is chosen and the corresponding natural frequency f_n, damping ratio ξ_n and normalized mode shape vector $\boldsymbol{\phi}_n$ are extracted. These modal triplets are then used in the next Chapter to track the evolution of the dynamic properties with increasing seismic input and damage.

4.6 Mode shape visualization

To interpret the identified modes, the modal vectors are visualized on the three-dimensional geometry of the buildings. Let $\mathbf{x}_j^0$ denote the coordinates of the j-th sensor location in the undeformed configuration and $\boldsymbol{\phi}_n$ the complex mode shape associated with mode n. A deformed configuration is obtained as

$$\mathbf{x}_j^{\text{def}} = \mathbf{x}_j^0 + \alpha\, \Re\{\boldsymbol{\phi}_{n,j}\}, \tag{4.7}$$

where α is a real scale factor chosen to improve visual clarity and $\boldsymbol{\phi}_{n,j}$ is the sub-vector of the modal shape associated with sensor j. The deformed frame is plotted together with the undeformed geometry, allowing for a direct visualization of global bending and torsional modes as well as the relative participation of the as-built and retrofitted buildings.

The same identification and visualization procedure is applied consistently to all white-noise tests considered in this thesis, providing a coherent basis for the comparison of modal properties across damage states and between the as-built and retrofitted specimens.

Chapter 5

Results of operational modal analysis

This chapter presents the results of the operational modal analysis (OMA) applied to the two full-scale RC buildings introduced in Chapter 3 and processed according to the methodology described in Chapter 4. The objectives are: (i) to illustrate how the global modes are identified from the white-noise (WN) tests; (ii) to track the evolution of natural frequencies and damping ratios with increasing seismic demand; and (iii) to compare the dynamic behavior of the as-built Building 1 and the retrofitted Building 2, as well as the experimental results with the STKO reference model.

Unless otherwise stated, all results refer to output-only identification from the white-noise excitations interleaved with the scaled Irpinia records, as summarized in Table 3.2. Modal parameters are estimated using both FDD/FSDD and SSI-COV, and a consistent set of modes is selected according to the stabilization criteria of Section 4.5.

5.1 Analyzed tests and twin-building configuration

The analysis considers the sequence of white-noise records WN2–WN7 recorded on 27–28/06/2022. WN2 and WN3 are low-amplitude signals acquired before any severe Irpinia excitation and are therefore representative of the initial, almost-undamaged state. WN4–WN7 are recorded after progressively stronger Irpinia runs (50%, 75%, 100% and 125% scaling), and are used to monitor the evolution of modal parameters as damage accumulates. For each white-noise record, OMA is carried out separately for Building 1 and Building 2.

The two test structures were designed as nominally twin RC frames. To make a fair comparison of their seismic performance, the additional mass of the energy-dissipation system was compensated by casting an extra 14 cm RC slab at the top floor of the other building, so that the total mass and gravity loads of the two specimens are practically the same. Therefore, differences in the identified modal properties between Building 1 (as-built) and Building 2 (retrofitted) can be mainly attributed to the presence of the

retrofit system and to the different damage evolution, rather than to mass asymmetries.

5.2 Identification of global modes

To illustrate the identification procedure, this section focuses on the white-noise record WN2, taken as reference state for both buildings. The figures reported here refer to Building 1; Building 2 shows the same pattern of modal peaks, shifted to slightly higher frequencies, and is therefore not reproduced for brevity.

5.2.1 Singular values and stabilization diagram

Figure 5.1 shows the singular values of the output PSD matrix obtained from FDD/FSDD for Building 1 under WN2. The first singular value (CMIF) exhibits three dominant peaks in the low-frequency range, corresponding to the first global lateral modes of the structure. Higher-frequency peaks are associated with local floor and panel deformations and are not further analyzed here.

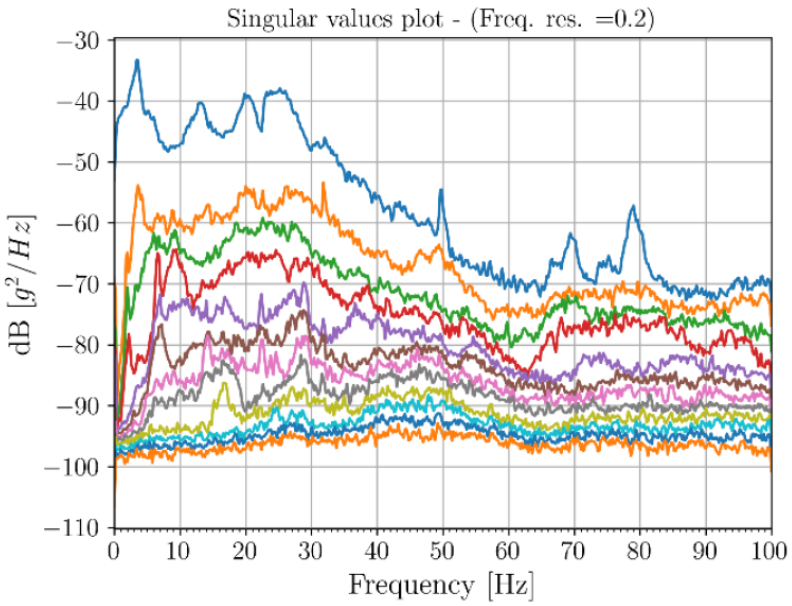

Figure 5.1: Building 1, White Noise 2: singular values of the output PSD matrix (FDD/FSDD). Peaks of the first singular value indicate candidate natural frequencies.

The corresponding SSI-COV stabilization diagram is reported in Fig. 5.2. Each marker represents an identified pole for a given model order, and the blue line shows again the first singular value from FDD/FSDD. Vertical alignments of stable poles (in terms of frequency, damping and mode shape) form clear clusters around the CMIF peaks. This combined inspection of singular values and stabilization diagrams follows standard OMA practice for civil structures [1, 13] and provides a first, qualitative identification of the natural frequencies.

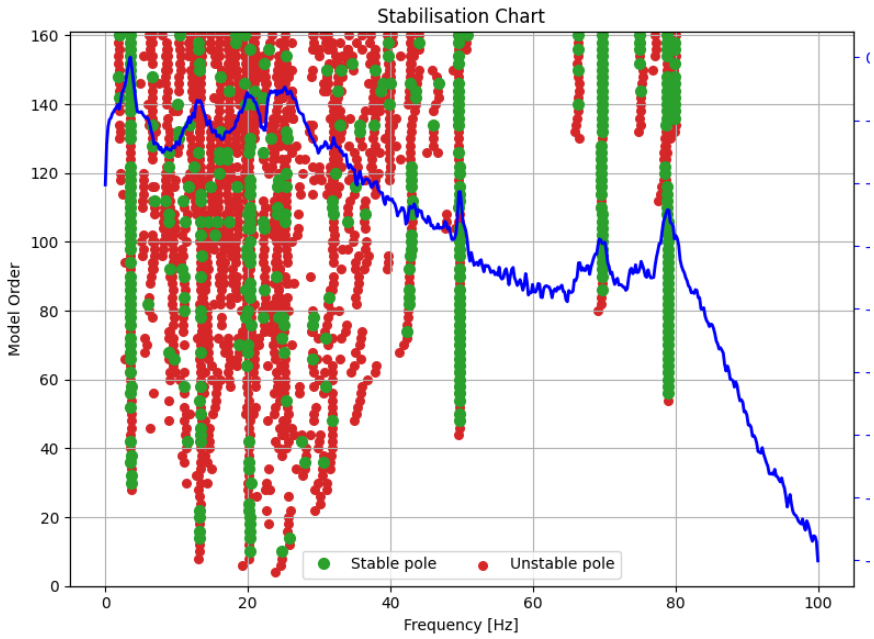

Figure 5.2: Building 1, White Noise 2: SSI-COV stabilization diagram with the first singular value (blue line). Vertical clusters of stable poles form in correspondence of the main CMIF peaks.

5.2.2 Frequency–damping clustering and reduced stabilization

A complementary view is provided by the frequency–damping plot in Fig. 5.3. Stable poles are highlighted in green, while unstable ones are shown in red. Stable poles aggregate into a limited number of frequency bands, with damping ratios typically between about 1% and 6%, which is consistent with the ranges reported in the literature for RC buildings under low-to-moderate vibration levels [1, 13]. Outliers with unrealistically high or low damping are discarded.

Finally, Fig. 5.4 shows a reduced stabilization diagram in which poles have been pre-filtered and color-coded according to automatic stability criteria (e.g. thresholds on relative changes of frequency, damping and MAC between successive model orders). This allows a more compact visualization of the frequency bands where stable poles persist over a wide range of model orders, and is particularly useful when dealing with a large number of poles, as in the present case [1].

By jointly inspecting the singular values (Fig. 5.1), the full and reduced stabilization diagrams (Figs. 5.2 and 5.4) and the frequency–damping clustering (Fig. 5.3), the natural frequencies retained for the subsequent analysis are selected as those: (i) corresponding to clear CMIF peaks; (ii) associated with vertical families of stable poles across several model orders; and (iii) lying in damping ranges compatible with RC building behavior. For Building 1, three global lateral modes are retained; for Building 2, four global modes are identified in the frequency range of interest.

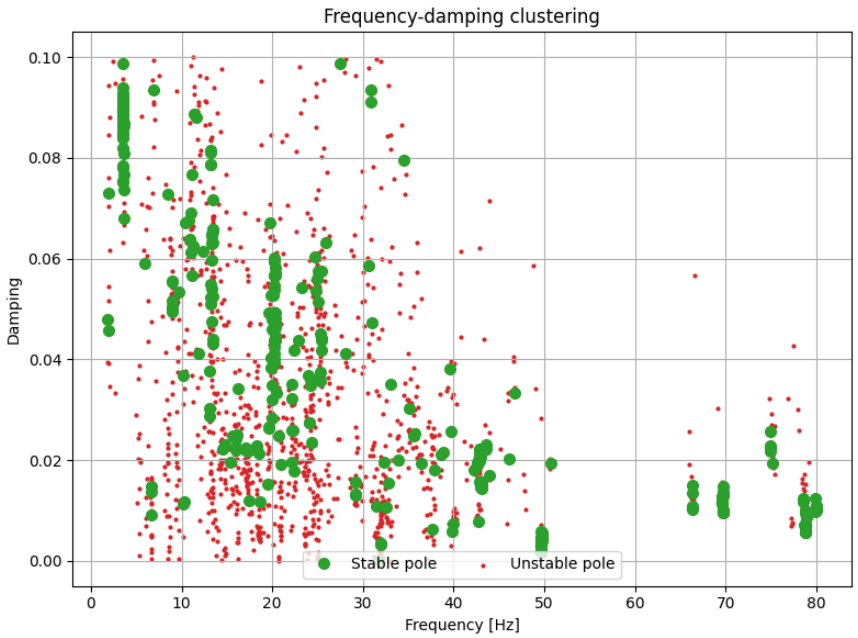

Figure 5.3: Building 1, White Noise 2: frequency–damping clustering of SSI-COV poles. Green markers denote poles classified as stable; red markers denote unstable poles. Stable clusters identify the frequency bands of the physical modes.

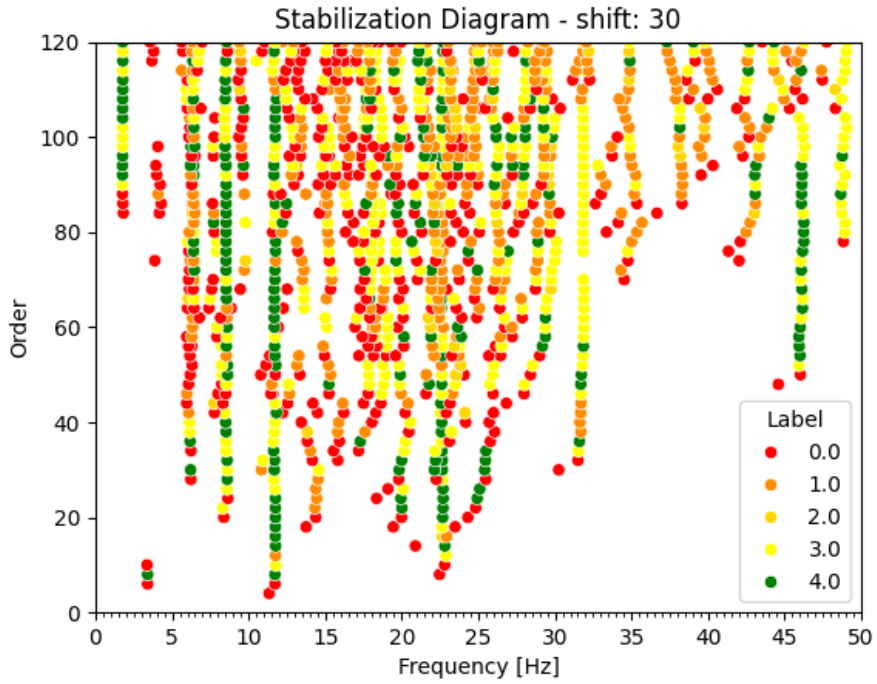

Figure 5.4: Building 1, White Noise 2: reduced stabilization diagram obtained from SSI-COV after applying the automatic stability criteria. The color label (0–4) denotes the stability class, with higher labels corresponding to poles that are stable in frequency, damping and mode shape.

5.3 Modal parameters from all white-noise tests

The modal parameters extracted according to the above criteria are summarized, for all white-noise tests, in Tables 5.1–5.2. For Building 1, the table also reports the relative frequency variation with respect to the STKO reference model, which represents the undamaged numerical baseline. The values listed are obtained from the Python implementation of the EFDD/FSDD and SSI-COV procedures described in Chapter 4; the MATLAB implementation is used as an independent check, but only one set of numerical values is reported here.

5.3.1 Building 1: frequency reduction and comparison with STKO

Table 5.1: OMA experimental results and comparison with the STKO reference model for Building 1. For each mode and white-noise test, f_n denotes the experimental natural frequency, ξ_n the equivalent viscous damping ratio, and Δf_n the relative frequency difference with respect to STKO, expressed in percent.

STKO f_n [Hz]	White Noise 2			White Noise 3			White Noise 4		
	f_n [Hz]	Δf_n [%]	ξ_n [%]	f_n [Hz]	Δf_n [%]	ξ_n [%]	f_n [Hz]	Δf_n [%]	ξ_n [%]
1.83	1.91	4.57	5.40	1.91	4.67	3.43	1.78	-2.57	3.55
5.84	6.63	13.59	1.21	6.68	14.45	1.10	6.46	10.66	2.11
8.31	8.98	8.02	5.26	8.96	7.86	5.01	8.53	2.59	4.16
STKO f_n [Hz]	White Noise 5			White Noise 6			White Noise 7		
	f_n [Hz]	Δf_n [%]	ξ_n [%]	f_n [Hz]	Δf_n [%]	ξ_n [%]	f_n [Hz]	Δf_n [%]	ξ_n [%]
1.83	1.63	-10.91	4.77	1.54	-15.57	2.93	1.51	-17.22	3.65
5.84	5.94	1.81	3.09	5.38	-7.74	4.16	5.1	-13.03	4.14
8.31	7.89	-5.02	3.32	7.15	-13.91	5.66	6.19	-25.51	3.79

At low excitation levels (WN2–WN3), the experimental frequencies are close to the STKO values, with $|\Delta f_n|$ typically below about 15%. This indicates that the FE model provides a reasonable representation of the elastic stiffness of the as-built frame in the initial state. The differences are compatible with the modeling simplifications and uncertainties in material properties usually encountered in full-scale tests [1, 3].

As the excitation level increases (WN4–WN7), all three modes show a clear, monotonic reduction in frequency, with Δf_n becoming increasingly negative. The largest drops occur after the 100% and 125% Irpinia runs, signaling significant stiffness degradation in the as-built frame. The magnitude of the frequency reduction is in line with values reported in the literature for RC buildings subjected to moderate-to-severe damage [1, 13].

Damping ratios generally increase along the test sequence, especially for Modes 2 and 3, reflecting the growth of hysteretic dissipation in the cracked RC members and joints. Estimated damping values remain within the broad interval typically observed in experimental databases for RC buildings [13].

5.3.2 Building 2: retrofitted configuration

For the retrofitted Building 2, no separate STKO model is considered, and the focus is on the experimental evolution of modal properties. The results are summarized in Table 5.2, which reports the identified natural frequencies and damping ratios for the first four global modes across all white-noise tests.

Table 5.2: OMA experimental results for Building 2. For each white-noise test, the table lists the identified natural frequencies f_n and equivalent viscous damping ratios ξ_n of the first four global modes.

White Noise 2			White Noise 3			White Noise 4		
Mode	f_n [Hz]	ξ_n [%]	Mode	f_n [Hz]	ξ_n [%]	Mode	f_n [Hz]	ξ_n [%]
1	2.37	2.41	1	2.37	1.36	1	2.19	2.21
2	-	-	2	-	-	2	4.33	5.47
3	7.62	2.38	3	7.63	1.66	3	6.94	3.25
4	11.81	5.51	4	-	-	4	10.53	3.36
White Noise 5			White Noise 6			White Noise 7		
Mode	f_n [Hz]	ξ_n [%]	Mode	f_n [Hz]	ξ_n [%]	Mode	f_n [Hz]	ξ_n [%]
1	1.98	1.83	1	1.74	2.61	1	1.63	2.44
2	3.80	4.41	2	3.43	5.03	2	3.15	5.00
3	6.49	6.56	3	5.85	5.37	3	5.38	3.65
4	9.34	4.26	4	8.17	4.53	4	7.52	3.93

Similar to Building 1, the frequencies of Building 2 decrease with increasing excitation, indicating stiffness degradation. However, the relative reductions are smaller, especially for the first bending mode, and the frequencies remain consistently higher than those of the as-built building for corresponding damage states. This behavior confirms that the retrofit system effectively increases and preserves the lateral stiffness under strong shaking.

Damping ratios of Building 2 show a moderate increase with damage, with somewhat higher values for the higher modes in the most severe tests. The overall levels are comparable with those of Building 1, suggesting that the retrofit primarily affects stiffness rather than introducing significant additional damping.

5.4 Consistency between Python and MATLAB implementations

As described in Chapter 4, the OMA procedure was implemented in two independent environments: a Python-based pipeline relying on PyOMA2 and a MATLAB-based pipeline using the original PyOMA/SSI functions. Both follow the same sequence of pre-processing, FDD/FSDD and SSI-COV identification.

For a representative subset of tests (including WN2, WN4 and WN5), the modal parameters obtained from the two implementations were compared. The identified

natural frequencies and damping ratios for the first global modes differ by only a few percent, and the corresponding mode shapes are visually very similar. This cross-check provides additional confidence in the robustness of the identification: in the remainder of this chapter, numerical values are reported from the Python implementation, while the MATLAB results are mainly used for mode-shape animations and MAC analysis.

5.5 Experimental mode shapes and comparison with the STKO model

5.5.1 White noise 2 mode shapes for Building 1

Figure 5.5 shows the first three experimental mode shapes of Building 1 identified from WN2 using the MATLAB-based SSI-COV analysis. The deformations are plotted on a simplified wire-frame representation of the structure, with the displacements scaled for clarity.

The first experimental mode at about 1.9 Hz is characterized by a global sway of the twin-frame system, but the predominant motion is oriented opposite to the nominal excitation direction. This apparently "reversed" behavior is consistent with the adopted sign convention and with the presence of the internal steel safety frame, which is bolted to the intermediate and top slabs and provides an additional, stiffer load path on the side opposite to the shaking direction. As a result, the coupled deformation of the RC frame and the steel frame leads to a stiffer response of the intermediate floor and a net lateral sway that appears oriented against the input direction. The second mode, around 6–7 Hz, shows a predominantly bending and torsional deformation about the vertical axis, while the third mode is a higher-order bending mode in the global X (shaking) direction, with increased deformation of the upper storeys. Despite the limited number of sensors per floor, these figures clearly confirm that WN2 excites the global lateral response of the twin-frame system.

5.5.2 Comparison with STKO reference modes

The STKO FEM reference model for Building 1 provides the undamaged numerical baseline. Its first modes, reported in Fig. 5.6, consist of a fundamental bending mode in the shaking direction, followed by a torsional mode and higher-order bending/torsional combinations.

A qualitative comparison between Figs. 5.5 and 5.6 shows that the experimental Modes 2 and 3 are in good agreement with the numerical torsional-bending and higher-order bending modes, in terms of both deformation pattern and relative storey participation. The fundamental experimental mode, however, deviates more significantly from the idealized first bending shape of the STKO model.

This discrepancy is attributed mainly to the presence of the internal steel safety

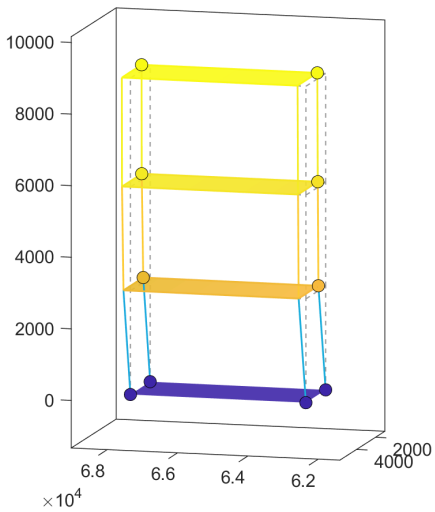

(a) Mode 1 – 1.90 Hz

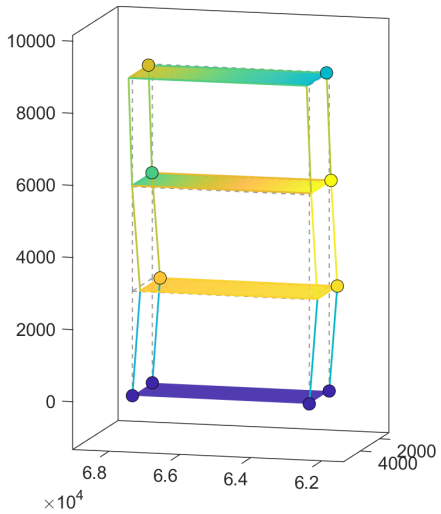

(b) Mode 2 – 6.60 Hz

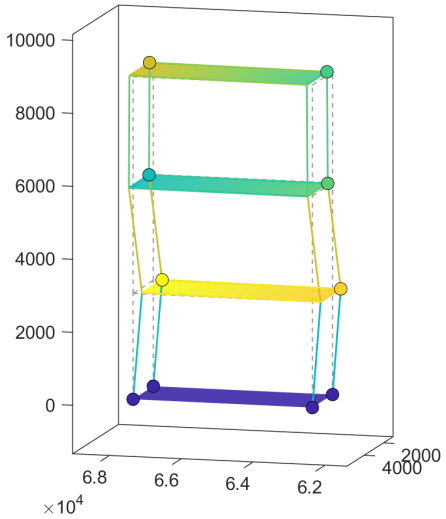

(c) Mode 3 – 8.98 Hz

Figure 5.5: Building 1, White Noise 2: experimental mode shapes identified with SSI–COV. The undeformed geometry is shown by dashed grey lines, while the colored slabs represent the deformed floors (displacements scaled for visualization).

frame used in the laboratory, which is bolted to the foundation slab and to the intermediate and top slabs (see chapter 3). The safety frame provides an additional load path and increases the lateral stiffness locally, especially at the mid-height of the specimen, but it is not explicitly represented in the STKO model. As a result, the first experimental mode from WN2 corresponds to a coupled deformation of the RC frame and the steel safety frame, whereas the STKO mode describes the bare RC frame only. Furthermore, the experimental mode shapes are reconstructed from a limited set of accelerometers, so they represent a spatially filtered approximation of the true continuous deformation.

A qualitative comparison between Figs. 5.5 and 5.6 shows that the experimental

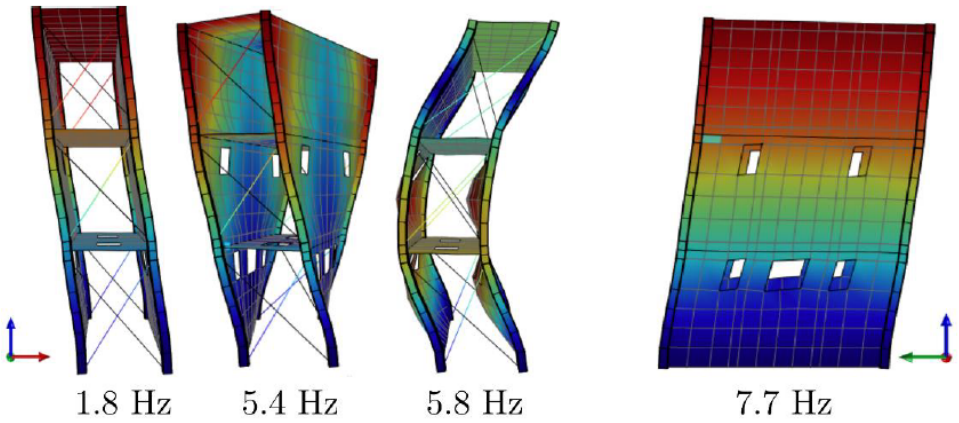

Figure 5.6: STKO FEM reference model for Building 1: visualization of the first four global mode shapes.

Table 5.3: STKO FEM reference modal analysis results for Building 1: natural frequencies and mass participation ratios.

Mode	f_n [Hz]	Mass participation [%]			Rot. mass participation [%]			Mode description
		Mass-X	Mass-Y	Mass-Z	Rot. X	Rot. Y	Rot. Z	
1	1.83	0.00	83.73	0.00	14.83	0.00	0.00	1st bending, Y direction
2	5.43	0.00	0.00	0.00	0.00	0.00	85.59	1st torsion
3	5.84	0.00	11.33	0.00	60.30	0.00	0.00	2nd torsion + bending Y
4	7.68	86.50	0.00	0.00	0.00	10.66	0.00	1st bending, X direction
5	8.31	0.00	1.65	0.00	6.02	0.00	0.00	Local 1st storey in phase
6	8.35	0.00	0.00	0.00	0.000015	0.00	0.00	Local 1st storey in counter-phase
Total		86.5	96.7	0.0	81.1	10.7	85.6	

Modes 2 and 3 are in good agreement with the numerical torsional-bending and higher-order bending modes, in terms of both deformation pattern and relative storey participation. The fundamental experimental mode, however, deviates more significantly from the idealized first bending shape of the STKO model.

This discrepancy is attributed mainly to the presence of the internal steel safety frame used in the laboratory, which is bolted to the foundation slab and to the intermediate and top slabs (see Chapter 3). The safety frame provides an additional load path and increases the lateral stiffness locally, especially at the mid-height of the specimen, but it is not explicitly represented in the STKO model. As a result, the first experimental mode from WN2 corresponds to a coupled deformation of the RC frame and the steel safety frame, whereas the STKO mode describes the bare RC frame only.

In addition, the numerical model idealizes the slabs as perfectly rigid diaphragms and neglects several secondary elements (e.g. non-structural components, connection details, added mass from cables and sensors), while the real structure exhibits finite

in-plane slab flexibility and local nonlinearities. These simplifications may lead to a different distribution of stiffness and mass and favor a stronger participation of the Y direction in the numerical first mode. Small differences in boundary conditions between the model and the test set-up (e.g. foundation restraint, interaction with the shaking table) can also influence the orientation and relative participation of the lowest modes.

Furthermore, the experimental mode shapes are reconstructed from a limited set of accelerometers, so they represent a spatially filtered approximation of the true continuous deformation. This spatial under-sampling, combined with measurement noise and the numerical noise inherent in the OMA algorithms, can mask local deformation patterns and slightly bias the apparent orientation of the experimental mode compared with the finely discretised FEM mode shape.

Despite these differences, the WN2 mode shapes confirm that the first three experimental modes are global lateral modes of the structure, and the frequencies reported in Table 5.1 remain reasonably close to the STKO predictions for the initial state. The more refined comparison of mode shapes, including quantitative MAC values, is therefore concentrated on those white-noise tests that provide the cleanest and most repeatable modal estimates, namely WN4 and WN5.

5.6 MAC-based assessment of mode separation and repeatability

5.6.1 Self-MAC: separation of experimental modes

To assess the degree of separation between the identified modes within a given test, the Modal Assurance Criterion (MAC) is computed between all pairs of normalized mode-shape vectors,

$$\mathrm{MAC}(\boldsymbol{\phi}_i, \boldsymbol{\phi}_j) = \frac{\left|\boldsymbol{\phi}_i^{\mathrm{H}} \boldsymbol{\phi}_j\right|^2}{\left(\boldsymbol{\phi}_i^{\mathrm{H}} \boldsymbol{\phi}_i\right)\left(\boldsymbol{\phi}_j^{\mathrm{H}} \boldsymbol{\phi}_j\right)}.$$

A value of MAC = 1.0 corresponds to a 100% match between two mode shapes (they are identical up to a scale factor), whereas MAC = 0.9 means a 90% correlation, typically considered an excellent match in OMA practice. Values around 0.0 indicate that the corresponding mode shapes are essentially orthogonal and therefore well separated.

Figures 5.7 shows the self-MAC matrices for Building 1 for White Noise tests WN2 to WN7 (MATLAB-based SSI-COV identification). Each matrix reports the MAC between the first three global modes of the same test.

For the lower-to-moderate excitation levels (WN2–WN5), the diagonal entries are equal to 1.00 and the off-diagonal terms remain very small (typically below 0.1). This corresponds to 100% self-correlation on the diagonal and less than 10% correlation between different modes, indicating that the three global modes are very well separated and that there is almost no mixing between their modal vectors.

As the excitation level increases (WN6) a slight degradation of the separation can

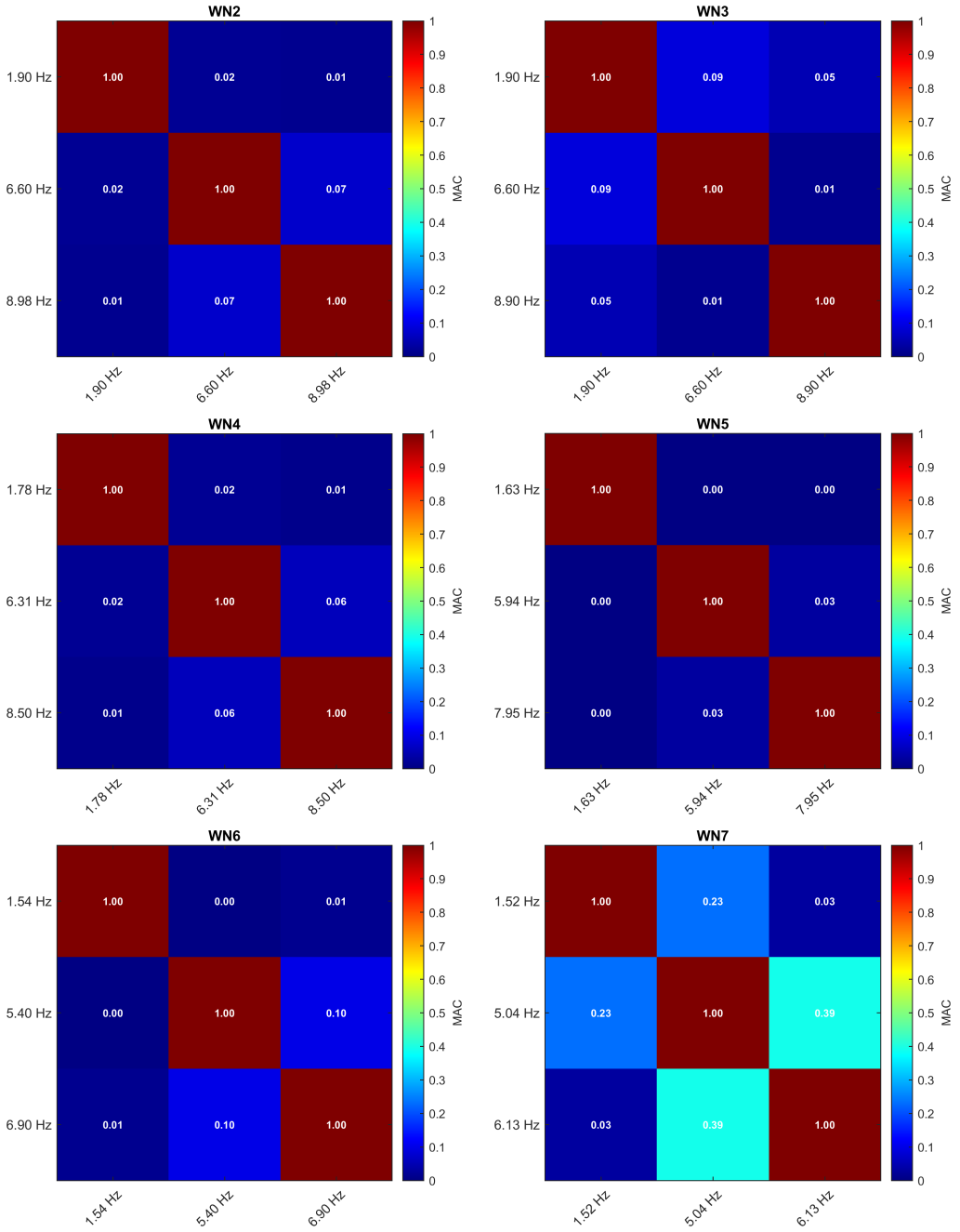

Figure 5.7: Building 1: self-MAC matrices of the identified mode shapes for White Noise tests WN2–WN7 (MATLAB implementation).

be observed that the diagonal MAC values remain equal to 1.00, but some off-diagonal terms grow to around 0.10, i.e. about 10% correlation between distinct modes. This suggests that the modes are still clearly distinguishable, but the increased response amplitude starts to enhance coupling effects and sensitivity to non-ideal boundary conditions.

For the highest excitation level (WN7), the loss of separation becomes more evident. While the diagonal elements are still equal to 1.00 (100% self-correlation), some off-diagonal entries reach values around 0.23–0.39, corresponding to 23–39% correlation between different modes. In other words, the modes are no longer perfectly orthogonal: their shapes are partially mixed, which is consistent with the structure having undergone significant cracking and stiffness degradation.

Overall, the sequence from WN2 to WN7 shows a gradual evolution: at low excitation the modes are almost perfectly separated, whereas at the highest excitation the separation is clearly less perfect. This behaviour supports the interpretation that the strongest excitations have modified the dynamic properties of the structure, and that the changes observed in the modal vectors at WN7 are a genuine signature of damage rather than purely an identification artefact.

5.6.2 Inter-test MAC: repeatability across excitation levels

To quantify the repeatability of the identified modal vectors across different white-noise levels, an inter-test MAC is computed between modes extracted from pairs of tests. Since WN4 and WN5 provide the cleanest stabilization diagrams and self-MAC matrices, they are used as the main reference for this comparison.

Figure 5.8 reports the MAC values between the mode shapes of Building 1 identified from WN4 and WN5 for the first three global modes. Values remain high (typically above about 0.9) for all three modes, indicating that the shapes are very similar despite the different excitation levels and damage states.

The cross-MAC matrix in Figure 5.8 shows very high diagonal values (0.99, 0.98 and 0.91) and negligible off-diagonal terms. A MAC value of 0.9 corresponds to a 90% correlation between two mode shapes and is typically regarded as an excellent match in operational modal analysis. Therefore, the diagonal values confirm that the three global modes are consistently identified between White Noise 4 and White Noise 5, while the near-zero off-diagonal entries indicate good separation between different modes.

An analogous cross-MAC matrix can be constructed for Building 2, again showing high inter-test MAC values for the first few modes. These results confirm that, within the range of moderate excitations represented by WN4 and WN5, the global mode shapes are robust and repeatable, and that the observed trends in frequency and damping in Tables 5.1 and 5.2 are not an artefact of inconsistent identification.

For combinations involving the lowest (WN2) and highest (WN7) excitation levels, the inter-test MAC values decrease, especially for the higher modes. This behavior

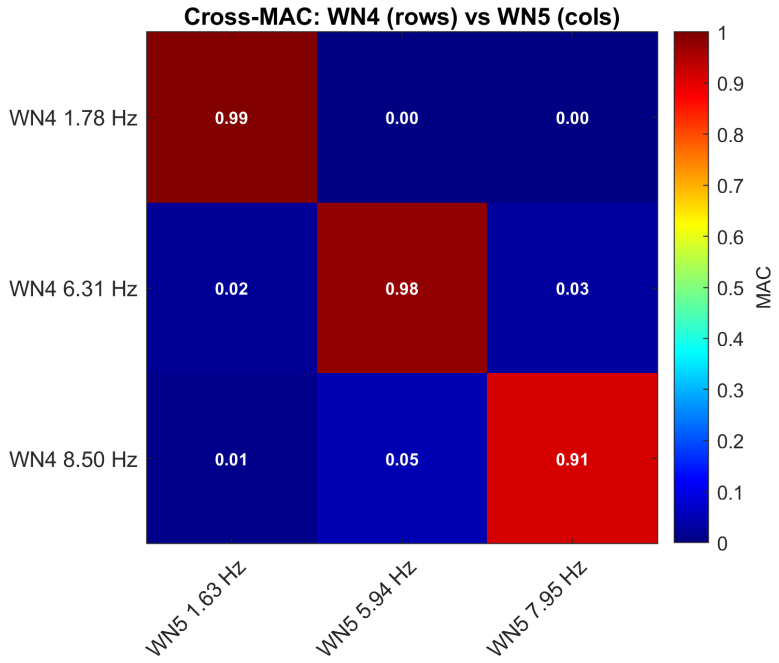

Figure 5.8: Cross-MAC matrix between mode shapes identified from White Noise 4 and White Noise 5, MATLAB implementation.

is consistent with physical expectations which at very low amplitudes, measurement noise and boundary-condition effects play a larger role, while at very high amplitudes the progressive cracking and stiffness degradation lead to genuine changes in the modal vectors. The high MAC values observed between WN4 and WN5 therefore represent a favorable "window" where the structure is sufficiently excited but still behaves close to linear, and are used as the main reference for the subsequent qualitative discussion of mode shapes and retrofit effectiveness.

Chapter 6

Discussion, conclusions and future developments

This chapter synthesizes the main findings of the work, answers the research questions posed in Chapter 1 and discusses the implications for operational modal analysis (OMA) and structural health monitoring (SHM) of reinforced concrete (RC) buildings. The results are interpreted in the broader context of OMA-based seismic protection, with particular reference to the framework proposed by Rainieri for combining OMA, finite element (FE) modelling and SHM in earthquake-prone regions [1, 13].

The chapter is organised as follows. Section 6.1 summarises the answers to the research questions (RQ1–RQ5) and evaluates the extent to which the objectives (O1–O5) have been met. Section 6.2 positions the case study within the existing OMA/SHM landscape, including links to automated OMA (AOMA). Section 6.3 formulates practical recommendations for OMA-based damage tracking in building-scale applications. Section 6.4 discusses limitations of the present work. Section 6.5 outlines directions for future research.

6.1 Synthesis of findings with respect to the research questions

6.1.1 RQ1 – Evolution of natural frequencies and damping with seismic demand and damage

RQ1 asked how the natural frequencies and damping ratios of the two buildings evolve under increasing seismic demand and accumulated damage, and to what extent these trends are robust indicators of stiffness degradation.

The OMA results from the white-noise tests WN2–WN7 show a clear and physically consistent evolution of the modal properties. For Building 1 (as-built configuration), the first three global modes identified at low excitation (WN2–WN3) have frequencies close to the STKO reference values, with deviations mostly within about 5–15%, indicating a

reasonable undamaged baseline. As the Irpinia 1980 record [9] is applied at increasing scaling levels, all three modes undergo a monotonic reduction in frequency. The first bending mode decreases from approximately 1.9 Hz in the initial state to about 1.5 Hz at WN7, corresponding to a relative reduction greater than 15% with respect to the numerical baseline. Higher modes show comparable or even larger relative drops. These trends are consistent with cumulative stiffness loss in the cracked RC members and connections and fall within the broad ranges reported in the OMA literature for RC buildings subjected to moderate-to-severe damage [3, 6, 7, 8].

The damping ratios of Building 1 generally increase along the test sequence, particularly for the second and third modes, reflecting growing hysteretic dissipation as damage accrues. Nevertheless, the identified damping values remain within the wide interval (roughly 1–7%) commonly observed in experimental databases for RC buildings and other civil structures [12, 37, 35, 29]. This confirms the well-known difficulty of using damping as a precise quantitative damage proxy.

For Building 2 (retrofitted configuration), the same qualitative pattern is observed: frequencies decrease with increasing excitation and damage, and damping ratios tend to grow slightly. However, the frequency reductions are smaller than in Building 1, and at matched damage states the frequencies remain consistently higher than those of the as-built building. This confirms that natural-frequency tracking is a robust indicator of stiffness degradation and retrofit effectiveness, whereas damping should be used more cautiously, primarily as a supporting measure rather than a primary damage index. Overall, RQ1 can be answered positively: OMA-based frequency trends, evaluated over a carefully designed test sequence, provide a clear and interpretable picture of stiffness loss in full-scale RC buildings.

6.1.2 RQ2 – Effectiveness of the retrofit system in terms of global stiffness and its degradation

RQ2 focused on the comparative performance of the as-built Building 1 and the retrofitted Building 2, asking whether the retrofit system increases global lateral stiffness and slows down stiffness degradation under strong shaking.

At the initial state (WN2–WN3), the first bending frequency of Building 2 is around 2.37 Hz, compared to about 1.91 Hz for Building 1, i.e. roughly 20–25% higher. This difference cannot be attributed to mass asymmetries, which were compensated by the additional top slab on the as-built frame; it therefore reflects a genuine increase in lateral stiffness due to the retrofit system. As the excitations become more severe, Building 2 also exhibits frequency reductions, signalling damage and stiffness loss, but the relative drops are smaller than for Building 1 and the absolute frequencies remain higher at all observed damage states.

In terms of damping, Building 2 shows modest increases with damage, especially for higher modes in the most severe tests. The overall damping levels are comparable

to those of Building 1, suggesting that the retrofit primarily acts on stiffness rather than introducing large additional energy dissipation. This is consistent with the design philosophy of many stiffness-increasing retrofit systems and with previous OMA-based retrofit assessments in RC buildings [3, 13]. Taken together, these observations support a positive answer to RQ2: the retrofit system increases and better preserves the global lateral stiffness of the frame under strong shaking, as evidenced by the higher and more stable natural frequencies across the test sequence.

6.1.3 RQ3 – Consistency between Python and MATLAB implementations

RQ3 investigated whether two independent OMA toolchains, a Python-based pipeline using PyOMA2 and related tools [11, 33] and a MATLAB-based pipeline using the OoMA and FDD toolboxes [38, 39], yield consistent modal parameters when applied to the same dataset and identification settings.

For representative tests (e.g. WN2, WN4, WN5), the natural frequencies and damping ratios identified with the Python and MATLAB implementations differ by only a few percent. The small numerical discrepancies are within the typical variability expected from different numerical implementations, windowing choices and post-processing details [25, 26, 30].

This cross-validation directly addresses O3 and gives confidence that the main conclusions of the thesis do not depend on a particular software environment. It also reinforces the view, emphasised by Rainieri and co-workers, that independent checks and consistent parameter settings are important for assessing the robustness of OMA results in SHM applications [1, 2, 13].

6.1.4 RQ4 – Ability of a reduced FE model to support interpretation of modes and stiffness changes

RQ4 asked how well a simplified FE model (STKO/OpenSees) can explain the observed modal characteristics and their evolution, and how modes should be paired when their order changes or when experimental modes are influenced by auxiliary elements such as the safety frame.

The comparison between STKO and experimental results shows that at low excitation levels the FE frequencies provide a reasonable baseline: deviations of the order of 5–15% are consistent with common modeling uncertainties in full-scale tests. Modes 2 and 3 of Building 1 at WN2 match well the numerical torsional and higher-order bending modes in terms of deformation pattern and storey participation, while the first mode exhibits a more pronounced discrepancy, mainly due to the unmodeled steel safety frame and idealized boundary conditions.

Despite these limitations, the FE model remains a valuable interpretative tool. It helps classify experimental modes (bending vs. torsion, global vs. local) and link

measured frequency reductions to approximate stiffness loss in the main lateral system. This role, using OMA and FE model updating in a complementary way, with the methodology applied to real structures. In this thesis, mode pairing is carried out using MAC-based criteria and qualitative inspection of mode shapes, allowing consistent tracking of mode families even when the order shifts with damage. RQ4 is therefore answered in a qualified way which a reduced FE model, suitably interpreted, is sufficient to support mode classification and stiffness trends, but care is required in the presence of auxiliary structural elements and modeling simplifications.

6.1.5 RQ5 – Influence of the internal steel safety frame and implications for SHM

RQ5 examined the influence of the internal steel safety frame on the identified modal properties and asked how this bias can be detected, quantified and accounted for when drawing SHM conclusions.

The analyses clearly show that the safety frame affects both mode shapes and, to a lesser extent, baseline frequencies. The first experimental mode at WN2, for example, exhibits a global sway with an apparent lateral deformation opposite to the nominal shaking direction, consistent with the presence of a stiff load path provided by the steel frame on the opposite side. The safety frame is not modelled in STKO, which contributes to the mismatch between the numerical first bending mode and the experimental fundamental mode.

Self-MAC and inter-test MAC analyses provide a quantitative way to assess the separation and repeatability of mode shapes across tests. For intermediate excitation levels (WN4–WN5), MAC values remain high (around ≈ 0.9) for the first three global modes, indicating well-separated and repeatable mode shapes, whereas at the lowest and highest excitation levels the MAC values degrade, reflecting larger sensitivity to boundary conditions and damage-induced nonlinearities [12, 37, 29].

From an SHM standpoint, the safety frame acts as a systematic bias that primarily affects mode shapes and boundary conditions, while the inter-test frequency trends between white-noise windows remain relatively robust. This justifies the decision to base the primary damage indicators on global frequency changes and cross-method consistency, treating shapes mainly as qualitative support. The findings provide a concrete answer to RQ5 and highlight the importance of explicitly documenting and, where possible, modelling auxiliary elements in laboratory campaigns and real structures [1, 13].

6.1.6 Summary with respect to the objectives O1–O5

The above findings can be summarised in terms of the specific objectives:

- **O1 (data pipeline and quality checks)** has been met through the development of a reproducible workflow for handling dense MEMS sensor data, including

orientation to the global frame, time synchronisation, anti-alias filtering, resampling and stationarity checks, following best practices in digital signal processing and OMA [15, 13, 12].

- **O2 (estimation of frequencies and damping via FDD and covariance-driven SSI)** is achieved by applying these methods consistently across WN2–WN7 and reporting trends via stable clusters and clustering criteria. The use of FDD/FSDD [34, 36] and covariance-driven SSI-COV [21, 22, 19, 27] is in line with the state of the art.

- **O3 (toolchain comparison)** is satisfied by the close agreement between PyOMA2 and MATLAB/OoMA results, thereby validating the open-source Python pipeline [33, 11, 38, 39].

- **O4 (reduced FE baseline and MAC-based mode pairing)** is fulfilled by using the STKO model to interpret mode types and mode participation and by pairing experimental and numerical modes through qualitative patterns and MAC information, consistent with model-based OMA studies on real structures [13, 3].

- **O5 (quantifying and controlling the influence of the steel safety frame)** is addressed by systematically discussing its role in shape distortions and boundary-condition effects, and by focusing primary conclusions on robust frequency trends.

6.2 Positioning within the OMA and SHM landscape

Rainieri's work [1, 2, 13] systematically demonstrates the reliability and versatility of OMA techniques across a range of structures and emphasises their role in seismic protection when combined with FE modelling and SHM systems. The present work can be viewed as a focused contribution within this broader framework, centred on a particularly well-instrumented, full-scale RC twin-building test under controlled seismic and white-noise excitations.

Several elements directly mirror the methodology and philosophy advocated in [1, 13]:

- **Integration of OMA and FE models.** In both this thesis and [1, 13, 3], OMA is used not only to identify modal parameters but also to support FE model assessment and interpretation. While [1] exploits OMA for both test design and model refinement of complex existing structures, this thesis uses a reduced STKO model as an interpretative baseline for stiffness and mode-type classification in a controlled laboratory setting.

- **Emphasis on data quality and processing choices.** The importance of record length, noise levels, hardware selection and processing parameters (e.g. block rows in SSI) for obtaining reliable estimates, particularly of damping, is

highlighted in [13, 12, 30, 28]. The present work explicitly designs the white-noise windows, applies careful preprocessing and fixes SSI parameters to ensure stability and comparability of the results.

- **Towards automated OMA and SHM.** Fully automated identification and tracking algorithms have been proposed and validated in the recent AOMA literature [4, 32, 31, 42]. In a complementary way, this thesis applies a structured, script-based pipeline in PyOMA2 to a large dataset, moves towards reproducible batch processing, and employs automatic stability criteria and clustering strategies that are compatible with automated OMA concepts.

From this perspective, the twin-building campaign and its analysis provide a high-quality dataset and a transparent pipeline that could serve as a benchmark or testbed for future automated OMA procedures, especially in the context of RC frame structures and retrofit evaluation.

6.3 Practical recommendations for OMA-based seismic damage tracking

Based on the case study and insights from the OMA/SHM literature, several practical recommendations can be formulated for applying OMA to seismic damage tracking in RC buildings:

1. **Design the excitation protocol to bracket damage states.** Interleaving broadband white-noise windows with scaled earthquake records, as done in the Irpinia–WN sequence, allows modal properties to be sampled at multiple damage states while approximately satisfying the stochastic-input assumptions of OMA [20, 13].

2. **Invest in data quality and preprocessing.** Dense MEMS sensor networks require careful attention to sensor orientation, time synchronisation and anti-alias filtering. Record length and signal-to-noise ratio are critical, particularly for damping estimation [10, 15, 12, 28].

3. **Combine frequency- and time-domain methods.** Using FDD/FSDD for initial frequency and mode-shape estimates and covariance-driven SSI for refined modal parameters and stabilisation diagrams provides complementary views on the same underlying dynamics [34, 36, 21, 19]. Joint inspection of CMIF peaks, stabilisation diagrams and frequency–damping clusters improves the robustness of mode selection.

4. **Prioritise frequencies as primary damage indicators.** For RC frames, global frequency shifts across repeated tests are generally more robust and easier

to interpret than damping changes or fine details of mode shapes, especially when boundary conditions and auxiliary elements (e.g. safety frames) are imperfectly known [6, 7, 40, 41].

5. **Use mode shapes and MAC as qualitative and consistency checks.** Mode shapes are valuable for distinguishing bending and torsional modes, detecting coupling effects and identifying bias from secondary structures, but their quantitative use should rely on self-MAC and inter-test MAC analyses to avoid over-interpreting noisy or under-sampled shapes [37, 29, 13].

6. **Maintain a simple but representative FE model.** Even a reduced-order FE model can significantly aid interpretation of experimental results, support mode pairing and inform stiffness-loss estimates, provided that key structural features and boundary conditions are captured [13, 3, 41]. FE models should be used iteratively, in the spirit of model updating for seismic assessment.

6.4 Limitations of the present work

The conclusions of this thesis should be interpreted in light of several limitations:

- **Single structural typology and loading protocol.** The study focuses on two nominally identical, single-bay, three-storey RC frames subjected to a specific earthquake record (Irpinia 1980) at scaled intensities [9]. The findings may not directly generalise to other structural typologies, irregular geometries or different ground motions.

- **Presence of the steel safety frame.** The internal steel frame, while essential for protecting the specimens and equipment, introduces boundary-condition complexity and mode-shape distortions that are only partially controlled. It is absent from the FE model and cannot be fully separated from the RC response in the experimental modes.

- **Limited exploration of damping and higher modes.** Although damping ratios are estimated and broadly interpreted, no detailed sensitivity study is performed on damping estimation settings (e.g. record length, block rows, windowing), which several authors identify as a key step towards more reliable damping use in SHM [13, 12, 28]. Moreover, the analysis concentrates on the first few global modes, leaving local and higher-frequency modes largely unexplored.

- **Finite dataset and laboratory conditions.** The results are based on a finite number of white-noise windows over a limited number of test days in a laboratory environment. Long-term environmental variability, aftershock sequences and operational conditions typical of real buildings are not captured [2, 37].

- **Toolchain scope.** The identification uses FDD/FSDD and covariance-driven SSI within PyOMA2 and OoMA. Other potentially informative algorithms available in the OMA toolbox—including refined parametric or automated procedures [25, 4, 32, 31, 42]—are not exploited here, in order to maintain focus and comparability.

These limitations suggest caution in extrapolating the numerical values beyond the present setup, while not undermining the qualitative lessons for OMA-based damage tracking.

6.5 Future research directions

The work opens several avenues for further research, many of which resonate with the open issues and future research topics discussed in [1, 13, 12, 14, 16]:

1. **Towards standard procedures for damping estimation.** Building on the current dataset, a systematic study could investigate the sensitivity of damping estimates to record length, number of block rows, windowing and noise levels, using multiple identification methods and uncertainty quantification frameworks [28, 30, 29]. This would directly address the need, highlighted in [13, 12], for standardised protocols and better understanding of damping mechanisms and uncertainties.

2. **Extension to continuous and long-term monitoring.** The hardware and the PyOMA2-based pipeline could be extended to continuous or near real-time monitoring of real buildings, integrating automated identification and tracking procedures similar in spirit to those proposed in [2, 4, 31, 32, 42]. This would provide a natural testbed for AOMA and for studying the interplay of environmental variability, operational loads and seismic events.

3. **Building and sharing modal property databases.** The present results could be incorporated into a larger database of modal parameters (frequencies, damping ratios, mode shapes) for RC structures under different excitation levels and damage states. Such databases, as suggested in [13, 14, 37], are essential for defining typical ranges, detecting anomalous values and refining SHM strategies and design criteria.

4. **Refined FE modelling and model updating.** Future work could develop more detailed FE models that explicitly include the steel safety frame, slab flexibility, non-structural components and non-linear behaviour [3, 41]. Model updating based on the full suite of experimental modes, possibly including higher modes and local deformations, would bring the analysis closer to the advanced seismic assessment strategies applied in complex, existing structures [1, 13].

5. **From frequency trends to quantitative damage indices.** While this thesis focuses on qualitative stiffness loss inferred from frequency reductions, future research could explicitly link modal changes to damage indices, residual capacity and performance-based assessment metrics, possibly leveraging probabilistic or machine-learning approaches [14, 16, 40, 42].

6. **Automation and user-independent decision steps.** Several decision points in the current workflow—such as the selection of stable poles, clustering thresholds and mode pairing—still require expert judgment. Extending PyOMA2 with robust, validated criteria for these steps would contribute to fully automated pipelines, addressing one of the main drawbacks identified for the widespread use of OMA in SHM: the need for extensive user interaction [13, 4, 32, 31].

In summary, this thesis has demonstrated that carefully designed OMA campaigns, combined with transparent data processing and simple but informative FE models, can provide rich insight into the seismic response, damage evolution and retrofit performance of RC buildings. The case study of the twin-building shake-table tests, interpreted within the broader framework established by Rainieri and others [1, 13, 14, 12], suggests that OMA will continue to play a central role in the development of SHM strategies for seismic risk reduction, especially as automated identification and monitoring tools mature and are deployed at scale.

Bibliography

[1] Carlo Rainieri. "Operational Modal Analysis for Seismic Protection of Structures". PhD thesis. Naples, Italy: University of Naples "Federico II", 2008. DOI: 10.6092/unina/fedoa/3475. URL: https://doi.org/10.6092/unina/fedoa/3475 (cit. on pp. 1, 3, 6, 50, 53, 58, 59, 61, 71, 73–75, 78, 79).

[2] Carlo Rainieri, Giovanni Fabbrocino, Gaetano Manfredi, and Mauro Dolce. "Robust Output-Only Modal Identification and Monitoring of Buildings in the Presence of Dynamic Interactions for Rapid Post-Earthquake Emergency Management". In: *Engineering Structures* 34 (2012), pp. 436–446. DOI: 10.1016/j.engstruct.2011.10.001. URL: https://doi.org/10.1016/j.engstruct.2011.10.001 (cit. on pp. 1–6, 73, 75, 77, 78).

[3] Fabrizio Gara, Sandro Carbonari, Daniele Roia, Alberto Balducci, and Laura Dezi. "Seismic Retrofit Assessment of a School Building through Operational Modal Analysis and FE Modeling". In: *Journal of Structural Engineering* 147.1 (2021), p. 04020302. DOI: 10.1061/(ASCE)ST.1943-541X.0002865. URL: https://doi.org/10.1061/(ASCE)ST.1943-541X.0002865 (cit. on pp. 1, 2, 5, 61, 72, 73, 75, 77, 78).

[4] Mario M. Rosso, Alessandro Aloisio, Jakub Parol, Giuseppe Carlo Marano, and Giuseppe Quaranta. "Intelligent Automatic Operational Modal Analysis". In: *Mechanical Systems and Signal Processing* 201 (2023), p. 110669. DOI: 10.1016/j.ymssp.2023.110669. URL: https://doi.org/10.1016/j.ymssp.2023.110669 (cit. on pp. 1–5, 76, 78, 79).

[5] Kai Zhou and Q. S. Li. "Modal Identification of High-Rise Buildings under Earthquake Excitations via an Improved Subspace Methodology". In: *Journal of Building Engineering* 52 (2022), p. 104373. DOI: 10.1016/j.jobe.2022.104373. URL: https://doi.org/10.1016/j.jobe.2022.104373 (cit. on pp. 1–4).

[6] Rodrigo Astroza, Hamed Ebrahimian, Joel P. Conte, José I. Restrepo, and Tara C. Hutchinson. "Statistical Analysis of the Modal Properties of a Seismically-Damaged Five-Story RC Building Identified Using Ambient Vibration Data". In: *Journal of Building Engineering* 52 (2022), p. 104411. DOI: 10.1016/j.jobe.2022.104411. URL: https://doi.org/10.1016/j.jobe.2022.104411 (cit. on pp. 2, 6, 72, 77).

[7] Chun-Man Liao. "Modal and Wave Propagation Analysis of Vibration Tests on a Laboratory Building Model Before and After Damage". In: *Structural Control and Health Monitoring* 2025.1 (2025), p. 3453150. DOI: 10.1155/stc/3453150. URL: https://doi.org/10.1155/stc/3453150 (cit. on pp. 2, 72, 77).

[8] Giovanni Rebecchi, Paolo M. Calvi, Alberto Bussini, Filippo Dacarro, Davide Bolognini, Luca Grottoli, Matteo Rosti, Francesco Ripamonti, and Stefano Cii. "Full-Scale Shake Table Tests of a Reinforced Concrete Building Equipped with a Novel Servo-Hydraulic Active Mass Damper". In: *Journal of Earthquake Engineering* 27.10 (2023), pp. 2702–2725. DOI: 10.1080/13632469.2022.2121338. URL: https://doi.org/10.1080/13632469.2022.2121338 (cit. on pp. 2, 6, 43, 72).

[9] F. Vaccari, P. Suhadolc, and G. F. Panza. "Irpinia, Italy, 1980 Earthquake: Waveform Modelling of Strong Motion Data". In: *Geophysical Journal International* 101.3 (1990), pp. 631–647. DOI: 10.1111/j.1365-246X.1990.tb05575.x. URL: https://doi.org/10.1111/j.1365-246X.1990.tb05575.x (cit. on pp. 6, 45, 72, 77).

[10] S. PalChaudhuri, A. K. Saha, and David B. Johnson. "Adaptive Clock Synchronization in Sensor Networks". In: *Proceedings of the Third International Symposium on Information Processing in Sensor Networks (IPSN 2004)*. ACM, 2004, pp. 340–348. DOI: 10.1145/984622.984672. URL: https://doi.org/10.1145/984622.984672 (cit. on pp. 3–5, 44, 47, 50, 76).

[11] Danilo P. Pasca, Diego F. Margoni, Marco M. Rosso, and Angelo Aloisio. "PyOMA2: An Open-Source Python Software for Operational Modal Analysis". In: *Proceedings of the 10th International Operational Modal Analysis Conference (IOMAC 2024)*. Vol. 307. Lecture Notes in Civil Engineering. Cham: Springer, 2024, pp. 423–434. DOI: 10.1007/978-3-031-61421-7_42. URL: https://doi.org/10.1007/978-3-031-61421-7_42 (cit. on pp. 3–6, 35, 73, 75).

[12] R. Brincker and C. Ventura. *Introduction to Operational Modal Analysis*. John Wiley & Sons, 2015. DOI: 10.1002/9781118535141 (cit. on pp. 7–9, 13, 15, 16, 56, 72, 74–79).

[13] Carlo Rainieri and Giovanni Fabbrocino. *Operational Modal Analysis of Civil Engineering Structures*. Springer, 2014. DOI: 10.1007/978-1-4939-0767-0 (cit. on pp. 7–13, 16, 20–26, 28, 30–34, 37, 38, 55, 58, 59, 61, 71, 73–79).

[14] Charles R. Farrar and Keith Worden. *Structural Health Monitoring: A Machine Learning Perspective*. John Wiley & Sons, 2012. DOI: 10.1002/9781118443118 (cit. on pp. 8, 9, 11, 15, 78, 79).

[15] Alan V. Oppenheim and Ronald W. Schafer. *Digital Signal Processing*. MIT video course. Prentice-Hall, 1975. ISBN: 9780132146357. URL: https://books.google.it/books?id=vfdSAAAAMAAJ (cit. on pp. 9–11, 75, 76).

[16] J.-A. Goulet. *Probabilistic Machine Learning for Civil Engineers*. MIT Press Ltd, 2020. ISBN: 9780262538701. URL: https://profs.polymtl.ca/jagoulet/Site/Goulet_web_page_BOOK.html (cit. on pp. 12, 78, 79).

[17] Anil K. Chopra. *Dynamics of Structures (in SI Units)*. 5th ed. Pearson Education, 2019. ISBN: 9781292249209. URL: https://books.google.it/books?id=Z76GEAAAQBAJ (cit. on p. 16).

[18] Benjamin Greiner. "Operational Modal Analysis and its Application for SOFIA Telescope Assembly Vibration Measurements". Study thesis; online published 2010. MA thesis. Deutsches SOFIA Institut, 2009. URL: http://nbn-resolving.de/urn:nbn:de:bsz:93-opus-50403 (cit. on pp. 15, 16).

[19] Peter Van Overschee and Bart De Moor. *Subspace Identification for Linear Systems: Theory—Implementation—Applications*. Springer, 2012. DOI: 10.1007/978-1-4613-0465-4 (cit. on pp. 19, 20, 22, 28, 31, 34, 55, 75, 76).

[20] P. Mohanty and Daniel J. Rixen. "Operational modal analysis in the presence of harmonic excitation". In: *Journal of Sound and Vibration* 270.1-2 (2004), pp. 93–109. DOI: 10.1016/S0022-460X(03)00485-1 (cit. on pp. 21, 76).

[21] Shaker R. Ibrahim and Edward C. Mikulcik. "A method for the direct identification of vibration parameters from the free response". In: *Shock and Vibration Bulletin*. Part 4. The Shock and Vibration Information Center; September 1977. 1977. URL: https://ntrs.nasa.gov/citations/19800070016 (cit. on pp. 21, 75, 76).

[22] Jer-Nan Juang and Richard S. Pappa. "An eigensystem realization algorithm for modal parameter identification and model reduction". In: *Journal of Guidance, Control, and Dynamics* 8.5 (1985), pp. 620–627. DOI: 10.2514/3.20031 (cit. on pp. 21, 34, 75).

[23] B. Ho and R. E. Kálmán. "Effective construction of linear state-variable models from input/output functions: Die Konstruktion von linearen Modellen in der Darstellung durch Zustandsvariable aus den Beziehungen für Ein- und Ausgangsgrößen". In: *at - Automatisierungstechnik* 14.1-12 (1966), pp. 545–548. DOI: 10.1524/auto.1966.14.112.545 (cit. on p. 22).

[24] Minh Phan, Jer-Nan Juang, and Richard W. Longman. *On Markov Parameters in System Identification*. Technical report. NASA, 1991. URL: https://ntrs.nasa.gov/api/citations/19920004241/downloads/19920004241.pdf (cit. on p. 21).

[25] J.-H. Yi and C.-B. Yun. "Comparative study on modal identification methods using output-only information". In: *Structural Engineering and Mechanics: An International Journal* 17.3 (2004), pp. 445–466. DOI: 10.12989/sem.2004.17.3_4.445 (cit. on pp. 24, 73, 78).

[26] K. A. Kvåle, O. Øiseth, and A. Rönnquist. "Covariance-driven stochastic subspace identification of an end-supported pontoon bridge under varying environmental conditions". In: *Dynamics of Civil Structures, Volume 2: Proceedings of the 35th IMAC, A Conference and Exposition on Structural Dynamics 2017*. Springer, 2017, pp. 107–115. DOI: 10.1007/978-3-319-54777-0_14 (cit. on pp. 24, 25, 73).

[27] M. Döhler and L. Mevel. "Modular subspace-based system identification from multisetup measurements". In: *IEEE Transactions on Automatic Control* 57.11 (2012), pp. 2951–2956. DOI: 10.1109/TAC.2012.2193711 (cit. on pp. 24, 36, 75).

[28] V. A. A. Yeny, I. D. G. Araújo, J. D. Villalba-Morales, and L. A. A. Aracayo. "Validation of the uncertainty bounds on modal parameters identified with the SSI-COV method". In: *Latin American Journal of Solids and Structures* 18 (2021). DOI: 10.1590/1679-78256725 (cit. on pp. 24, 76–78).

[29] J. Lardiès. "Modal parameter identification from output data only". In: *MATEC Web of Conferences* 20 (2015), p. 01002. DOI: 10.1051/matecconf/20152001002 (cit. on pp. 24, 72, 74, 77, 78).

[30] Shuai Li, Jin-Ting Wang, Ai-Yun Jin, and Guang-Heng Luo. "Parametric analysis of SSI algorithm in modal identification of high arch dams". In: *Soil Dynamics and Earthquake Engineering* 129 (2020), p. 105929. DOI: 10.1016/j.soildyn.2019.105929 (cit. on pp. 25, 73, 76, 78).

[31] Y. V. Ardila, I. D. Gómez-Araújo, and J. D. Villalba-Morales. "An Automated Procedure for Continuous Dynamic Monitoring of Structures: Theory and Validation". In: *Journal of Vibration Engineering & Technologies* 12.3 (2023), pp. 4463–4482. DOI: 10.1007/s42417-023-01121-1 (cit. on pp. 26, 76, 78, 79).

[32] G. Zini, M. Betti, and G. Bartoli. "A quality-based automated procedure for operational modal analysis". In: *Mechanical Systems and Signal Processing* 164 (2022), p. 108173. DOI: 10.1016/j.ymssp.2021.108173 (cit. on pp. 26, 76, 78, 79).

[33] Danilo P. Pasca, Alessandro Aloisio, Mario M. Rosso, and Sotirios Sotiropoulos. "PyOMA and PyOMA_GUI: A Python module and software for Operational Modal Analysis". In: *SoftwareX* 20 (2022), p. 101216. DOI: 10.1016/j.softx.2022.101216 (cit. on pp. 33, 34, 73, 75).

[34] Rune Brincker, Lingmi Zhang, and Palle Andersen. "Modal identification of output-only systems using frequency domain decomposition". In: *Smart Materials and Structures* 10.3 (2001). DOI: 10.1088/0964-1726/10/3/303 (cit. on pp. 34, 55, 75, 76).

[35] Rune Brincker, Claudio E. Ventura, and Palle Andersen. "Damping estimation by frequency domain decomposition". In: *Proceedings of IMAC 19: A Conference on Structural Dynamics*. Hyatt Orlando, Kissimmee, Florida: Society for Experimental Mechanics, Feb. 2001. URL: https://vbn.aau.dk/en/publications/2bcee690-9c2e-11db-8ed6-000ea68e967b (cit. on pp. 34, 72).

[36] L. Zhang, T. Wang, and Y. Tamura. "A frequency–spatial domain decomposition (FSDD) method for operational modal analysis". In: *Mechanical Systems and Signal Processing* 24.5 (2010). DOI: 10.1016/j.ymssp.2009.10.024 (cit. on pp. 34, 55, 75, 76).

[37] Bart Peeters. "System Identification and Damage Detection in Civil Engineering". PhD thesis. Katholieke Universiteit te Leuven, 2000. URL: https://lirias.kuleuven.be/1725571&lang=en (cit. on pp. 34, 55, 72, 74, 77, 78).

[38] Andrew Otto. *OoMA Toolbox*. https://www.mathworks.com/matlabcentral/fileexchange/68657-ooma-toolbox. MATLAB Central File Exchange, retrieved 16 November 2025. 2025 (cit. on pp. 38, 39, 73, 75).

[39] Mohammad Farshchin. *Frequency Domain Decomposition (FDD)*. https://www.mathworks.com/matlabcentral/fileexchange/50988-frequency-domain-decomposition-fdd. MATLAB Central File Exchange, retrieved 16 November 2025. 2015 (cit. on pp. 38, 39, 73, 75).

[40] Sina Zolfagharysaravi, Denis Bogomolov, Camilla Bahia Larocca, Federica Zonzini, Lorenzo Mistral Peppi, Marco Lovecchio, Luca De Marchi, and Alessandro Marzani. "ARMA Model for Tracking Accelerated Corrosion Damage in a Steel Beam". In: *Sensors* 25.8 (2025). DOI: 10.3390/s25082384. URL: https://doi.org/10.3390/s25082384 (cit. on pp. 39, 77, 79).

[41] Amthal Hakim, Wael Slika, Rawan Machmouchi, and Adel Elkordi. "Numerical Approach to Simulate the Effect of Corrosion Damage on the Natural Frequency of Reinforced Concrete Structures". In: *Structural Durability & Health Monitoring* 17.3 (2023). DOI: 10.32604/sdhm.2022.023027. URL: https://www.techscience.com/sdhm/v17n3/53293 (cit. on pp. 39, 77, 78).

[42] Alessandro Cardoni, Amir Reza Elahi, and Gian Paolo Cimellaro. "A Refined Output-Only Modal Identification Technique for Structural Health Monitoring of Civil Infrastructures". In: *Engineering Structures* 323 (2025). DOI: 10.1016/j.engstruct.2024.119210. URL: https://doi.org/10.1016/j.engstruct.2024.119210 (cit. on pp. 39, 76, 78, 79).